



**Altimetry, gravimetry, GPS and viscoelastic modelling data for the joint inversion for
glacial isostatic adjustment in Antarctica (ESA STSE Project REGINA)**

3

Ingo Sasgen¹, Alba Martín-Español², Alexander Horvath³, Volker Klemann⁴, Elizabeth J.
Petrie⁵, Bert Wouters⁶, Martin Horvath⁷, Roland Pail³, Jonathan L. Bamber², Peter J.
6 Clarke⁸, Hannes Konrad⁹, Terry Wilson¹⁰ and Mark R. Drinkwater¹¹

9

1. Division of Climate Sciences, Alfred Wegener Institute, Bussestraße 24, 27570
Bremerhaven, Germany.

2. School of Geographical Sciences, University of Bristol, University Road, Clifton,
Bristol BS8 1SS, United Kingdom.

12

3. Institut für Astronomische und Physikalische Geodäsie, Technische Universität
München, Arcisstraße 21, 80333 München, Germany.

15

4. Department of Geodesy, GFZ German Research Centre for Geosciences,
Telegrafenberg, 14473 Potsdam, Germany.

5. School of Geographical and Earth Sciences, University of Glasgow, Glasgow, G12
8QQ, United Kingdom.

18

6. Institute for Marine and Atmospheric Research, Utrecht University, Princetonplein 5,
3584 CC, Utrecht, The Netherlands.

21

7. Institut für Planetare Geodäsie, Technische Universität Dresden, Helmholtzstr. 10,
01069 Dresden, Germany.

8. School of Civil Engineering and Geosciences, Newcastle University, Newcastle, NE1
7RU, United Kingdom.



24 9. School of Earth and Environment, University of Leeds, Leeds, LS2 9JT, United Kingdom.

27 10. School of Earth Science, Ohio State University, 275 Mendenhall Lab, 125 South Oval Mall, Columbus OH, 43210, USA.

11. Mission Science Division, European Space Agency, European Space Research and Technology Centre, Keplerlaan 1, Noordwijk 2201 AZ, The Netherlands.

30

Keywords:

Global change from geodesy, Gravity anomalies and Earth structure, Loading of the Earth,

33 Glaciology, Antarctica, Joint inversion



ABSTRACT

36 A major uncertainty in determining the mass balance of the Antarctic ice sheet from
measurements of satellite gravimetry, and to a lesser extent satellite altimetry, is the poorly
known correction for the ongoing deformation of the solid Earth caused by glacial isostatic
39 adjustment (GIA). In the past decade, much progress has been made in consistently modelling
the ice sheet and solid Earth interactions; however, forward-modelling solutions of GIA in
Antarctica remain uncertain due to the sparsity of constraints on the ice sheet evolution, as well
42 as the Earth's rheological properties. An alternative approach towards estimating GIA is the
joint inversion of multiple satellite data – namely, satellite gravimetry, satellite altimetry and
GPS, which reflect, with different sensitivities, trends of recent glacial changes and GIA.
45 Crucial to the success of this approach is the accuracy of the space-geodetic data sets. Here, we
present reprocessed rates of surface-ice elevation change (Envisat/ICESat; 2003-2009), gravity
field change (GRACE; 2003-2009) and bedrock uplift (GPS; 1995-2013.7). The data analysis
48 is complemented by the forward-modelling of viscoelastic response functions to disc load
forcing, allowing us to relate GIA-induced surface displacements with gravity changes for
different rheological parameters of the solid Earth. The data and modelling results presented
51 here are available in the Pangeae archive; <https://doi.pangaea.de/10.1594/PANGAEA.875745>.
The data sets are the input streams for the joint inversion estimate of present-day ice-mass
change and GIA, focusing on Antarctica. However, the methods, code and data provided in this
54 paper are applicable to solve other problems, such as volume balances of the Antarctic ice sheet,
or to other geographical regions, in the case of the viscoelastic response functions. This paper
presents the first of two contributions summarizing the work carried out within a European
57 Space Agency funded study, REGINA.



COPYRIGHT STATEMENT

60 The work presented here is provided under the terms of the Creative Commons License

Attribution 3.0 Unported (CC BY 3.0).



63 1. INTRODUCTION

Glacial isostatic adjustment (GIA), the viscoelastic deformation of the solid Earth in response to climate-driven ice and water mass redistribution on its surface, is poorly constrained
66 in Antarctica. The primary reason is the sparseness of geological evidence of the past ice sheet geometry and local relative sea-level change. These are important constraints on the exerted glacial forcing and on the viscoelastic structure of the lithosphere and of the mantle,
69 respectively, which concertedly determine the signature of GIA (e.g. Peltier, 2004; Ivins and James 2005; Whitehouse et al. 2012; van der Wal et al., 2015). The predictions of GIA in Antarctica remain ambiguous (Shepherd et al. 2012, suppl.) and cause a large uncertainty in
72 gravimetric mass balance estimates of the ice sheet of the order of the estimate itself (Martín-Español et al. 2016b). Measurements of bedrock uplift by GPS have shown to be inconsistent with forward models, which tend to over-predict uplift and mass increase due to GIA, biasing
75 estimates of present-day Antarctic ice-mass loss from GRACE to more negative values (Bevis et al. 2009).

Much progress has been made in reconstructing the ice sheet evolution from
78 geomorphological evidence (Bentley et al. 2014) and inferring the underlying Earth structure from seismic observations (An et al. 2015; Heeszel et al. 2016). However, an independent approach to constraining GIA is to make use of the different sensitivities of the various types
81 of satellite data to recent glacial changes and GIA, respectively. And thus to separate both signals in a joint inversion approach has been pursued by e.g. Wahr et al. 2000; Riva et al. 2009; Wu et al. 2010; Gunter et al. 2014, Martín-Español et al. 2016a. Another approach used regional
84 patterns of GIA from forward modelling and adjusted them to GIA uplift rates in Antarctica (Sasgen et al. 2013).



In this paper, we present methods and data inputs in preparation of solving the joint
87 inversion for GIA in Antarctica. As the GIA process is gradual, causing an approximately
constant rate of change within a decade, we first process the satellite data to recover optimal
temporal linear trends. We refine existing procedures for the surface-ice elevation changes from
90 Envisat and ICESat satellite altimetry (Section 2), bedrock displacement from *in situ* networks
of GPS stations in Antarctica (Section 3), and gravity field change from GRACE (Section 4).
We also present forward modelling results of viscoelastic response functions to disc load forcing
93 for the range of Earth structures likely to prevail in Antarctica (Section 5).

The determination of viscoelastic response functions is a classic topic in solid Earth
modelling (e.g. Peltier & Andrews, 1976), though uncommon the application to joint invasion
96 studies of satellite data. Although this paper focusses on Antarctica, the response functions and
data processing techniques presented here are applicable to other regions. The response kernels
represent a wide range of Earth structures and can be used for the separation of superimposed
99 present-day (elastic) and past (viscoelastic) signatures of mass change in other regions, for
example hydrological storage changes and GIA in North America. The response functions give
insight into the temporal and spatial scales of deformation expected for Antarctica, and are
102 crucial when combining the input data streams.

The data sets and modelling results presented in this paper are accessible in the Pangaea
archive, <https://www.pangaea.de/> – subsections provide user guidance and point to data and
105 code stored in the archive. As mentioned above, the data sets and modelling results are of value
to address other research questions as well. For example, the GPS rates provided are useful for
the validation of forward modelling GIA solutions, the GRACE gravity rates can be used for
108 mass balance studies, and altimetry data 2003-2009 can be extended with the ongoing CryoSat-



2 mission to infer volumetric mass balances, also over the ice shelves. The viscoelastic response
functions are based on Earth model parameters suitable to other geographical regions, as well;
111 they are useful for similar studies combining different data sets of geodetic observables, surface
deformation, gravity field change, and topographic change in glaciated areas.

The actual method of the joint inversion is described in a second contribution of the
114 REGINA project team (Sasgen et al. *submitted*). In this second paper, the resulting GIA estimate
is also compared to previous studies. The processing of the data issued here was enabled by the
European Space Agency within the CryoSat+ Support To Science Element Study REGINA.

117



2. ALTIMETRY DATA ANALYSIS

2.1 ICESat elevation rate determination

120 We use along-track altimetry measurements from *ICESat 633 Level 2*, providing high-
resolution elevation change observations for the period February 2003 until October 2009. Two
corrections are applied to this data set: the range determination from Transmit-Pulse Reference-
123 Point Selection (Centroid vs. Gaussian) (Borsa et al. 2014) available from the National Snow
and Ice Data Center (NSIDC), and the inter-campaign correction (Hofton et al. 2013). The
Centroid-Gaussian correction is a well-established correction and has been incorporated to the
126 latest ICESat release (634). Concerning the ICESat Intercampaign Bias (ICB) correction,
uncertainties are available at Hofton et al (2013). Furthermore, several studies have determined
this correction from different methodologies. For a summary of published ICESat ICB
129 corrections see Scambos & Shumman (2016). Because ICESat tracks do not usually overlap, a
regression approach is used in which topographic slope (both across-track and along-track) and
the rate of surface-elevation change y_{ICESat}^h , are simultaneously estimated using the ‘plane’
132 method (Howat et al. 2008’) over areas spanning 700 m long and few hundred meters wide. A
regression is only performed if a plane has at least 10 points from four different tracks that span
at least one year. Regression was carried out twice; first, individual elevation measurements
135 with corresponding residuals outside the range of two standard deviations were detected, then,
the regression was repeated omitting these outliers. The standard deviation of the regression
coefficient, here taken as the uncertainty of the elevation rate, σ^h (here, ICESat) is calculated
138 by the propagation of the residual uncertainties of the topographic heights,

$$\hat{\sigma}_{ICESat} = \sqrt{\frac{\sum e_i^2 / (n-2)}{\sum (x_i - \bar{x})^2}}, \quad (1)$$



to the trend parameter, where \mathbf{e} is the vector of residuals, n is the sample size ($i =$
141 $1, 2, \dots, n$), and \mathbf{x} is the vector of input elevations with mean \bar{x} . This standard deviation (σ_{ICESat})
takes into account the sample size and the variance of both input data and residuals of the
regression (Hurkmans et al. 2012). The exact ICESat observation periods are shown in the
144 Appendix (A.1, Table A.1). Then, the elevation rate and its uncertainty are interpolated to a
common 10×10 km grid in polar-stereographic projection (central latitude 71°S ; central
longitude 0°W , and origin at the South Pole, WGS-84 reference ellipsoid).

147 2.2 Envisat elevation rate determination

We use a time series of elevation changes derived from along-track Envisat radar altimetry
data for the interval January 2003 to October 2009 (coeval to ICESat time span). Elevation
150 rates y_{Envisat}^h are obtained at points every 1 km along track, by binning all the echoes within a
500 m radius. Then, a 10-parameter least squares model is fitted in order to correct for the
across-track topography and changes in snowpack properties. The least square model is defined
153 in Flament and Remy (2012). The estimated parameters include parameters determined for the
backscatter, leading-edge width and tailing-edge slope, the mean altitude, quadratic surface
slope parameters to define surface curvature and a linear time trend. A digital elevation model
156 was not used for the correction of the topographic slope. For processing reasons, the temporal
resolution is re-sampled from 35 days to monthly periods for each grid cell, before estimating
the elevation rates. This has a minor effect on the elevation rate estimate (smaller than ± 1 cm)
159 and reduces the standard deviation by about 14 %. As for ICESat, the elevation rate is
interpolated to a common 10×10 km polar stereographic grid, and the standard deviations of
the rates within each grid cell are taken as an estimate of the measurement uncertainty, σ_{Envisat} .



162 2.3 *Combination of Envisat and ICESat*

We produce a combined rate of surface-elevation change product from the ICESat and
Envisat datasets for the Antarctic ice sheet, y^h . The aim is to take advantage of the high spatial
165 resolution of ICESat data and the high temporal resolution and high-track density of the Envisat
data.

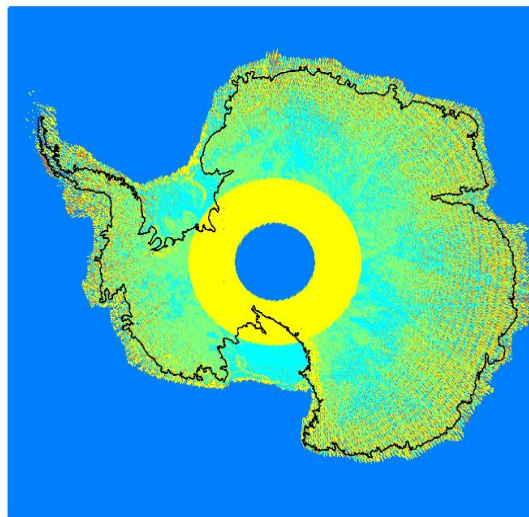


*Figure 1. Mask for the combination of Envisat/ICESat. ICESat but not Envisat available (yellow),
 $\sigma_{ICESat} \leq \sigma_{Envisat}$ (green), $\sigma_{ICESat} > \sigma_{Envisat}$ (turquoise), Envisat but not ICESat
available (orange), and no data (blue). No interpolation is used.*

We combine the two altimetry datasets based on their common 10×10 km polar-
168 stereographic grid. At each location, the elevation rate with the smallest standard deviation is
chosen from either Envisat or ICESat datasets.

Fig. 1 shows the resulting mask underlying the combination. It is evident that some grid
171 points are only represented by either ICESat or Envisat. Most prominent is the narrowing of the
polar gap with ICESat data, resulting from the 81.5°S latitude limit for Envisat compared to



86°S for ICESat due to satellite orbit inclination. On the Antarctic Peninsula, Envisat picks up
174 some points that are not present due to a sparser track coverage in the ICESat data set. As
expected, ICESat outperforms Envisat in terms of uncertainty of the elevation rate over steep
topographic slopes and along the ice sheet margins. This is due to the smaller footprint of the
177 laser altimeter, its higher accuracy and lower slope-dependent uncertainty (e.g. Brenner 2007).
On some flat areas and over some faulty ground tracks, where ICESat data measurements are
scarce, however, Envisat provides better temporal and spatial coverage leading to better
180 accuracy of the resulting elevation rates. The resulting combined data set of surface-elevation
rates and its uncertainties are shown in Fig. 2.

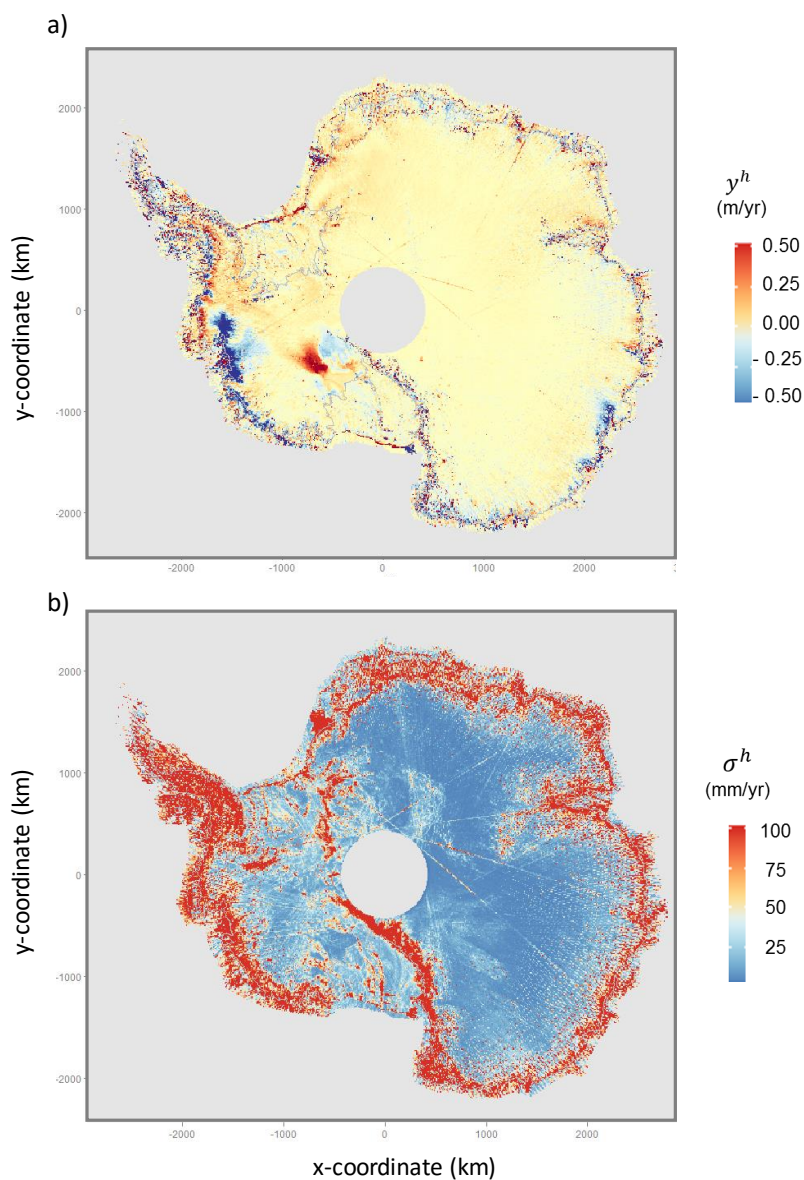


Figure 2: a) Rate of surface-ice elevation change y_h and b) associated uncertainties σ_h derived from Envisat/ICESat combined dataset for the time interval 2003-2009. No interpolation is used; grid points without values are empty (shaded grey).

183 2.4 *Firn correction*

The elevation rates derived from ICESat and Envisat are corrected for changes in the firn layer thickness using the firn compaction model of Ligtenberg (2011), which is driven by the regional atmosphere and climate model RACMO2/ANT (Lenaerts, 2010). We determine the firn compaction for January 2003 to October 2009, with respect to the mean of the years 1979 to 2002 and estimate a temporal linear trend, h_{comp} . The model output is re-gridded onto the 10 × 10 km common grid using nearest neighbor interpolation. The standard deviation of the re-gridding is less than 1 cm/yr, causing a maximum change of 2 % of the firn compaction rate. Note that the firn compaction model has a spatial resolution of 27 km, potentially neglecting finer-scale processes relevant for the altimetry data. Clearly, the re-gridding uncertainty stated above is merely a minimum estimate, neglecting, for example, uncertainties in the calibration or the atmospheric forcing of the firn compaction model.

The data were re-sampled from every two days to monthly mean time periods for every grid cell before estimating elevation rates. As for the Envisat and ICESat data, no seasonal terms are co-estimated and removed (i.e. annual and semi-annual). We do not apply an *a priori* correction for surface-mass balance (SMB) trends, in accordance with the GRACE processing (Section 5), which requires defining a climatological reference period. Note that applying the commonly used reference period (1979 to present) leads to spurious accumulation anomalies in the altimetry data (see Appendix A.2, Fig. A.1). The derivation of an adequate climatological reference epoch in the RACMO2/ANT simulations is in itself challenging and beyond the scope of this paper.

The total uncertainty of the rate of elevation change from satellite altimetry is calculated by



$$\sigma_h = \sqrt{\sigma_{\text{Envisat/ICESat}}^2 + \sigma_{\text{Firn}}^2}, \quad (2)$$

207 where the standard deviation of the firm correction, σ_{Firn} is the formal regression
uncertainty (neglecting model uncertainties, as these are not available), and we assume the error
sources to be uncorrelated.

210 2.5 Data availability

Annual elevation trends from a combination of Envisat and ICESat data for the time period
between February 2003 and October 2009. Trends have been corrected for firm densification
213 processes using RACMO2/ANT. Elevation trends are provided in a 20 km polar stereographic
grid (central meridian 0° , standard parallel 71° S) with respect to the WGS84 geoid. X and Y
are given in km, and the elevation rate and its standard deviation are given in m/yr.

216 2.5.1 *ICESat elevation trend for the time period between February 2003 and October
2009.*

The dataset is provided in a 10 km grid in polar stereographic projection (central meridian
219 0° , standard parallel 71° S) with respect to the WGS84 geoid. X and Y are given in km, and
the elevation rate and its standard deviation are given in m/yr.

222 2.5.2 *Envisat elevation trend for the time period between February 2003 and October
2009.*

The dataset is provided in a 10 km grid in polar stereographic projection (central meridian
 0° , standard parallel 71° S) with respect to the WGS84 geoid. X and Y are given in km, and the
225 elevation rate and its standard deviation are given in m/yr.



2.5.3 ICESat & Envisat combination for time period between February 2003 and October
2009.

228 Elevation changes have been corrected for firm densification processes using a FDM. The
dataset is provided in a 10 km grid in polar stereographic projection (central meridian 0°
standard parallel 71° S) with respect to the WGS84 geoid. X and Y are given in km, and the
231 elevation rate and its standard deviation are given in m/yr.

2.5.4 *Annual elevation trends from CryoSat-2 derived from a single trend covering the
time period 2010-2013.*

234 An acceleration term in areas with dynamic thinning was added to the linear trend to obtain
annual rates. Elevation trends are provided at 10 km resolution in a polar stereographic grid
(central meridian 0° , standard parallel 71° S) with respect to the WGS84 geoid. X and Y are
237 given in km and the elevation rate and its standard deviation are given in m/yr.

2.5.5 *Elevation changes from firm model*

Annual firm densification rates over 2003-2013 rates obtained from RACMO2.3. Data is
240 provided in a 27 km polar stereographic grid (central meridian 0° , standard parallel 71° S) with
respect to the WGS84 geoid. X and Y are given in km and the annual firm densification rates
in m/yr.

243 2.5.6 *Snow / ice density map*

The density map for volume-to-mass conversion is provided in 20 km resolution in a polar
stereographic grid (central meridian 0° , standard parallel 71° S) with respect to the WGS84
246 geoid. X and Y are given in km and density in km/m³.

2.5.7 *ICESat/Envisat combination mask*

Mask used for combining ICESat and Envisat in a 10 km resolution and polar stereographic



249 coordinates.

X and Y are coordinates in km and the id represents whether ICESat or Envisat has been used to construct the elevation change combination.

252 4: only Envisat was available

3: only ICESat was available

2: ICESat lower errors

255 1: Envisat lower errors

3. GPS UPLIFT RATE ESTIMATION & CLUSTERING

The aim of the GPS time series analysis is to derive uplift rates, y_u that represent the geophysical ground motion at the sites as accurately and robustly as possible. We derive uplift rates based on GPS records from a total of 118 Antarctic sites. Data were processed from 1995 day of year (doy) 002 to 2013 doy 257 (1995.0-2013.7) but data at individual sites are of varying length and quality. The processing and uplift rate and uncertainty estimation methodology are documented in detail in Petrie et al. (in prep. a, b), but a short summary is given here for convenience. It resembles that of Thomas et al. (2011), but with more recent processing software (GIPSY 6.2) and model updates (including second order ionospheric and earth radiation models): an initial satellite orbit and clock estimation step is performed, using a carefully selected balanced stable global network of GPS sites. The orbits and clocks are then used to perform precise point positioning (PPP) processing of all the available Antarctic sites of interest. A mini-ensemble was created to investigate systematic processing uncertainties and manual investigation was performed of effects of possible systematic errors in the time series on uplift rates. The mini-ensemble investigation showed that decisions taken when analyzing time series tended to have larger effects on uplift rates and uncertainties than the effects of small



processing strategy changes. Outliers and systematic errors, such as offsets due to equipment
273 changes or other causes, were removed where possible. Due to the varying characteristics of
the time series it was not possible to use the same approach at all sites. The strategy was as
follows (and is summarized in Appendix A.3, Fig. A.3). For sites with over 2000 days of data,
276 uplift rates and associated uncertainties were estimated using the CATS software (Williams
2008). We co-estimated a white-noise scale factor for the formal uncertainties, and a power-law
noise amplitude with the index fixed to -1 (flicker noise), along with the temporal linear trend
279 (rate), seasonal (annual and semi-annual) parameters, and sizes of the offsets (at the specified
epochs).

The median values of the white-noise scale factor and the power law noise amplitude,
282 derived from these long time series, were then used to propagate rates and uncertainties for the
shorter time series, for which CATS cannot produce reliable estimates. For the propagation, the
time series with fewer than 2000 epochs are additionally subdivided into two categories;
285 continuous sites (≥ 2.5 yr), for which periodic parameters are estimated in the propagation of
uncertainties, and very short continuous sites (< 2.5 yr) and campaign sites for which periodic
parameters are not estimated. For each campaign, 1 mm of noise was added when propagating
288 the uncertainties, to allow for tiny differences when re-setting up equipment.

Finally, for each site, the uplift rate γ^u and its uncertainty σ^u are assessed by manually
removing portions of the time series (for example deleting campaigns in turn). If the rate
291 changes by an amount larger than the propagated uncertainty for the site, the uncertainty is
assigned as \pm the maximum difference in rate, and the rate is adjusted, if necessary, to the values
of the most likely part of the range. Sites with only two campaigns were assigned an uncertainty
294 of ± 100 mm/yr, unless there was further evidence for or against the existence of systematic



errors.

Table 1 summarizes the rate estimation methods and the number of sites for each. For
297 further details and full information on individual rates and time series, see Petrie et al. (in prep
a) for a full description of the processing and ensemble evaluation, and Petrie et al. (in prep b)
for details of time series analysis and rate and uncertainty estimation. Table 1 shows the
300 numbers of sites at which each approach was taken. Further work was undertaken to combine
or ‘cluster’ the rates regionally for inclusion in the estimation process – see the REGINA Paper
II (Sasgen et al. *submitted.*) for details.



Table 1: Number of sites for each GPS uplift rate and uncertainty estimation method.

Rate and uncertainty estimation method	Number of sites (118 total)
CATS rate and uncertainty ('cats, cats')	18
CATS rate, manually increased uncertainty ('cats, eman')	2
Propagated rate and uncertainty ('prop, prop')	28
Propagated rate and manually increased uncertainty ('prop, eman')	50
Manually adjusted rate and manually increased uncertainty ('rman, eman')	20

Table 2. Uplift rates y^u and associated uncertainties σ^u (mm/yr) for selected GPS sites with more than 2000 epochs of data, compared to data published by Thomas et al. (2011) and Argus et al. (2014). Temporal components and noise characteristics are derived using the CATS software (Williams 2008), i.e. 'cats, cats' method.

Site	REGINA		Thomas et al. (2011)		Argus et al. (2014)	
	y^u	σ^u	y^u	σ^u	y^u	σ^u
cas1	1.5	0.2	1.2	0.4	1.7	0.8
crar	0.7	0.4	1.0	0.7	1.0	0.6
dum1	-0.3	0.3	-0.8	0.5	-0.2	0.8
maw1	-0.4	0.2	0.1	0.4	0.2	0.6
mcm4	0.8	0.2	0.7	0.4		
sctb	0.9	0.5	0.6	1.1		
syog	1.1	0.2	2.3	0.4	0.6	0.8
tnb1	0.1	0.5	-0.2	0.8	-0.4	1.0
vesl	0.4	0.3	1.1	0.5	1.5	0.8
McMurdo*					1.0	0.6

*Sites: crar-sctb-mcm4-mcmd

3.1 Comparison with existing results

Next, we briefly compare the uplift rates at individual sites (data span 1995.0-2013.7)



306 derived from the GPS processing described above with those available from three previous
 studies: Thomas et al. (2011) (data span 1995.0-2011.0), Argus et al. (2014) (data span 1994-
 2012) and the more geographically limited set of Wolstencroft et al. (2015) (data span 2006-
 309 late 2013, focused on Palmer Land). It should be noted that the REGINA and Wolstencroft et
 al. (2015) rates are in ITRF2008, the Thomas et al. (2011) rates are in ITRF2005 (which has
 negligible scale or translation differences to ITRF2008), and the Argus et al. (2014) rates are in
 312 a reference frame specific to the paper which they note yields 0.5 mm/yr more uplift than
 ITRF2008 at high southern latitudes.

Due to the large number of Antarctic sites, in total 118, we focus the comparison on the

Table 3. Uplift rates y^u and associated uncertainties σ^u (mm/yr) for selected GPS sites with fewer than 2000 epochs for data, compared to data published by Thomas et al. (2011) and Argus et al. (2014). Noise characteristics are derived median values from CATS software results for longer station records and propagated in the parameter estimation ('prop, prop' method). See Appendix A.4, Table A.2 for a full list of rates from this study.

Site	REGINA		Thomas et al. (2011)		Argus et al. (2014)	
	y^u	σ^u	y^u	σ^u	y^u	σ^u
belg	-1.4	0.7	3.0	1.5	0.8	2.4
dupt	11.5	1.1			12.4	2.5
fonp	13.5	1.8			14.8	3.4
frei	-4.4	0.7			-2.9	1.4
hugo	0.9	1.3			1.7	3.6
robi	8.7	1.5			8.7	3.2
roth	5.5	1.4			5.4	1.4
svea	1.3	1.1	2.1	2.0	1.7	2.9
vnad	4.4	1.1			5.2	2.5



315 uplift rates and uncertainties derived by the methods ‘cats, cats’ (Table 2) and ‘prop, prop’
(Table 3). Uplift rates resulting from our study are provided in Appendix A.4 for all sites (Table
A.2). Tables A.3 shows comparisons with the values of Thomas et al. (2011) and Argus et al.
318 (2014) for ‘prop, eman’ sites not shown in the main text. All uplift rates, y^u , are in mm/yr,
with uncertainties reflecting 1-sigma standard deviations, σ^u . Sites with particularly complex
non-linear time series such as those at O’Higgins (ohi2, ohig) and Palmer (palm) in the Antarctic
321 Peninsula are omitted here, as comparison with different studies is potentially misleading due
to the effects of different measurement time periods. Table 2 shows data for selected sites with
long time series, where uplift rate and uncertainty were derived using the CATS software
324 (Williams 2008). Uplift rates at the majority of the GPS sites agree within uncertainty, except
syog (Syowa), where the REGINA value is between that from the other two studies. The
uncertainty limits for the REGINA value and the Argus et al. (2014) just meet at 0.9 mm/yr,
327 even when allowing for the ~ 0.5 mm difference in reference frames, but the Thomas et al.
(2011) value does not. This may be due to the fact that Thomas et al. (2011) estimate two offsets
in the series. Table 3 shows uplift rate comparisons for sites where the ‘prop,prop’ method was
330 used; the noise characteristics are derived from median values from CATS software results for
longer site records and then propagated in the parameter estimation in which annual and semi-
annual parameters were also estimated along with the trend. Again, the rates agree within
333 uncertainty, except for site belg where there is a disagreement with Thomas et al. (2011). This
may be due to their shorter data span. Table 4 shows comparisons for sites where the REGINA
rates and uncertainties have been manually evaluated based on the spread of rates obtained by
336 sub-sampling the time series (‘rman’ method). There is a large difference (over 10 mm/yr) in
the values at capf (Cape Framnes) between the REGINA value (4.0 ± 1.4 mm/yr) and the Argus



et al. (2014) value (15.0 ± 4.2 mm/yr). Interestingly, the Wolstencroft et al. (2015) rate values
 339 for bean, gmez, Intk, mkib, and trve are all systematically higher than the REGINA values, by
 an average of just over 3 mm/yr, and the uncertainties we assigned are also several times larger.
 For more detailed analysis of rates and time series at individual sites, see Petrie et al. (in prep
 342 b).

Table 4. Uplift rates y^u and associated uncertainties σ^u (mm/yr) for selected sites where uplift rates are manually evaluated based on the spread of rates obtained by sub-sampling the time series ('rman' method), compared to data published by Thomas et al. (2011), Argus et al. (2014), Wolstencroft et al. (2015). See also 'rman' sites in Table Appendix A.4, Table A.2.

Site	REGINA		Thomas et al. (2011)		Argus et al. (2014)		Wolstencroft et al. (2015)	
	y^u	σ^u	y^u	σ^u	y^u	σ^u	y^u	σ^u
bren	3.1	1.1	3.9	1.6	2.1	3.7	3.2	0.8
capf	4.0	1.4			15.0	4.2		
dav1	-1.6	0.6	-0.9	0.5	-0.8	1.0		
mait	0.4	1.1	0.1	0.6	1.3	0.7		
mbl3	1.3	17.9	0.1	2.0				
bean	2.1	4.3					7.5	1.2
gmez	1.5	4.8					5.7	0.8
Intk	4.6	3.1					6.0	0.7
mkib	4.7	2.6					6.9	0.5
trve	2.5	5.6					4.7	0.6



345 3.2 *Data availability*

 3.2.1 *Bedrock uplift rates*

 Bedrock uplift rates derived for the REGINA project are available in the text file
348 “REGINA_rates_full.txt”, as presented in Table A.2 and A.3 of the Appendix A.4. The files
 “REGINA_rates_03-13.txt” and “REGINA_rates_03-09.txt” contain subsets of the data, with
 the temporal coverage limited to 2003-2013.5 and 2003-2009, respectively. The files are
351 organized as follows:

 Lon [°], Lat [°], uplift rate [mm/yr], uncertainty of the uplift rate [mm/yr], GPS site ID

 These *.txt files are the input to the clustering script described below. No elastic correction
354 has been applied.

 3.2.2 *Clustering script*

 In addition to the uplift rates for individual GPS sites, we provide a *bash* script “cluster.sh”
357 for clustering the heterogeneous data according to their geographic locations, for a pre-defined
 threshold value. The idea is to reduce stochastic and geophysical noise of neighboring stations
 in order to obtain uplift rates that are better regional representations for the length scale
360 recovered with GRACE (ca. 200 km). In an iterative procedure, the script selects neighboring
 sites within a threshold and calculates the weighted average of the uplift rates and a simple
 uplift of the stations locations. Input to the script are the REGINA rate files, specified in the
363 previous Section 3.2.1. Further details can be found in REGINA paper II (Sasgen et al.,
 submitted). Note that the script relies on the open-source program suite Generic Mapping Tools,
 <http://gmt.soest.hawaii.edu/> (Wessel et al. 2013). Similar clustering can be achieved with the
366 function *kmeans* in Matlab® or its open-source alternative GNU Octave.



3.2.3 GPS time series

The GPS time series were created as part of the RATES project, not solely the REGINA
369 study. They will be made available along with the detailed descriptions in Petrie et al. (in prep
b). The time series of vertical bedrock displacement will then be accessible here: [LINK].

4. GRAVIMETRY DATA ANALYSIS

372 We investigate the Release 5 (RL05) GRACE coefficients of the Centre for Space Research
(CSR; Bettadpur, 2012) and the German Research Centre for Geosciences (GFZ; Dahle, 2013),
provided up to spherical-harmonic degree and order $j_{max}=96$ and 90 respectively in the Science
375 Data System (SDS). For reasons of comparison, we adopt $j_{max}=90$ for both GRACE solutions.
A temporal linear trend in the ocean bottom pressure variations modeled by the atmospheric
and oceanic background models (GAD) was re-added to the monthly solutions, according the
378 GRACE Science and Data System recommendation (Dobslaw et al. 2013). The GRACE
coefficients C_{20} were replaced by estimates from Satellite Laser Ranging (SLR) provided by
Cheng et al. (2013). In our analysis we apply the cut-off degrees $j_{max}=50$, which has been
381 commonly used, as well as $j_{max} = 90$, which is considered experimental in terms of the
remaining signal content.

The determination of the rate of the gravity field change over Antarctica follows the scheme
384 sketched in Fig. 3. The rate of the gravity field change, expressed as equivalent water height
variations, is estimated in the spatial domain by adjusting a six-parameter function consisting
of a constant, a temporal linear trend and annual and semi-annual harmonic amplitudes. A
387 quadratic term was not co-estimated due to the project's focus on the rates (i.e. temporal linear
trends). It should be stated that including a quadratic term would slightly reduce the residual
uncertainties, particularly in the Amundsen Sea Sector, where an acceleration of mass balance



390 rates occurs that is not accounted for by interannual SMB variations of the ice sheet (see Section
4.2).

The post-processing of the GRACE coefficients follows three main steps:

393 *Step 1: Optimization of de-stripping filter*

Due to effects like the propagation of measurement noise and temporal aliasing, a large
proportion of the variations contained in the monthly solutions is related to noise. The noise of
396 the monthly solutions is lowest close to the pole and exhibits a characteristic north-south

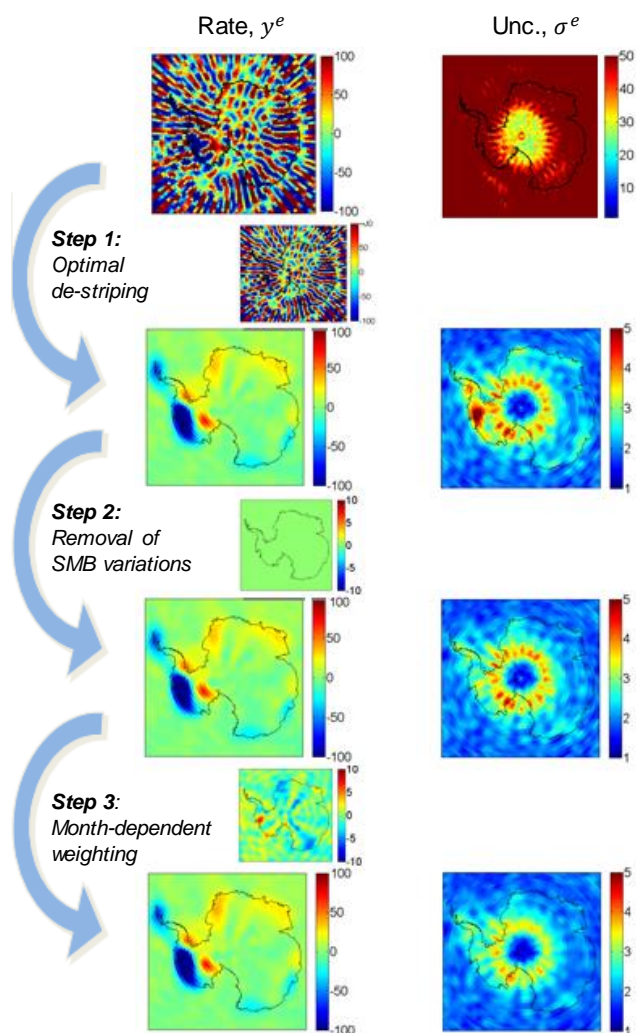


Figure 3. Post-processing steps applied to the GRACE gravity fields; shown is the impact on the gravity field rate y^g (left) and the associated RMS uncertainty σ^g (right). Small maps show change in the gravity field rate between two subsequent steps. Color scale is mm w.e./yr. GRACE data is GFZ RL05a.

oriented stripe pattern. This is visible in the gravity field rate and the propagated Root-Mean-Square (RMS) uncertainties shown in Fig. 3. In order to remove the stripe pattern, we apply the



399 de-correlation filter of Swenson & Wahr (2006) (hereinafter, “Swenson filter”) specifically
tuned to optimize the recovery of the gravity field rate over the region of Antarctica, which is
detailed in Section 4.1. Fig. 3 shows that the de-stripping procedure reduces the RMS uncertainty
402 of the rate by approximately one order of magnitude.

Step 2: Reduction of interannual mass variations

For isolating gravity field rates, the second step in the processing is the reduction of de-
405 trended variations of the surface mass balance, caused by accumulation events. The data set
used for this purposes is the RACMO2/ANT (Lenaerts et al 2012) converted into monthly sets
of spherical harmonic coefficients. The reduction of these interannual variations does not
408 change the temporal linear trend, but it reduces RMS uncertainties especially in coastal regions
(Fig. 3). Details are provided in Section 4.2.

Step 3: Month-dependent weighting

411 The performance of the GRACE satellite system was weaker in the early mission phase
due to issues with the star cameras of the satellites (*C. Dahle, GFZ, pers. comm.*; Fig. 5). A rate
estimate with uniform weighting of all months does not account for these variations. Therefore,
414 in the last step, month-dependent uncertainties are estimated and applied as weights during the
linear regression of the temporal linear trend. This slightly changes both the resulting rate
estimate, as well as its RMS uncertainties. Details are provided in Section 4.3.

417 Finally, after post-processing and evaluation of the gravity field rate (Section 4.4), we select
the GRACE release and cut-off degree providing the lowest uncertainty level (Section 4.5) as
reference input for our joint inversion for present-day ice-mass change detailed in REGINA
420 paper II (Sasgen et al. *submitted*).



4.1 Optimization of de-stripping filter

The Swenson filter has been proven to effectively reduce the typical north-south correlated
423 error structures of GRACE monthly solutions. The filter is based on the observation that these
structures correspond to correlated patterns in the spherical harmonic domain, namely
correlations within the coefficients of the same order and even degree, or respectively, odd
426 degree (Swenson & Wahr, 2006). The standard way of fitting and removing these patterns is by
adjusting polynomials to the respective sequences of spherical harmonic coefficients,
independently for individual months. Parameters to choose are the degree of the polynomial
429 n_{pol} and the minimum order m_{start} starting from which this procedure is applied. In principle,
a higher degree polynomial reduces the variability of coefficients of even / odd degree, and
results, also at lower minimum order, in stronger filtering – however, the behavior of the filter
432 may differ for regional applications, as discussed below. Note that tuning of other parameters
has been presented, e.g. the window width (Duan et al. 2009) or the degree range to which the
filter is applied. Chambers and Bonin (2012) have assessed these parameter options with regard
435 to the new GRACE RL05 solutions and global oceanic signals. Here, we perform a detailed
analysis of the choice of the Swenson filter parameters in order to optimize the signal-to-noise
characteristics of the rate of the gravity-field change over Antarctica. The resulting gravity field
438 rates are later used in the joint inversion for present-day ice-mass change and GIA described in
REGINA Part II.

We assess signal corruption by applying the filter to a synthetic test signal, which is based
441 on high-resolution elevation rates from satellite altimetry and reflects the prevailing signatures
of present-day ice-change with sufficient realism. For each choice of filter parameters, the
signal corruption is assessed as the RMS difference between the original and the filtered

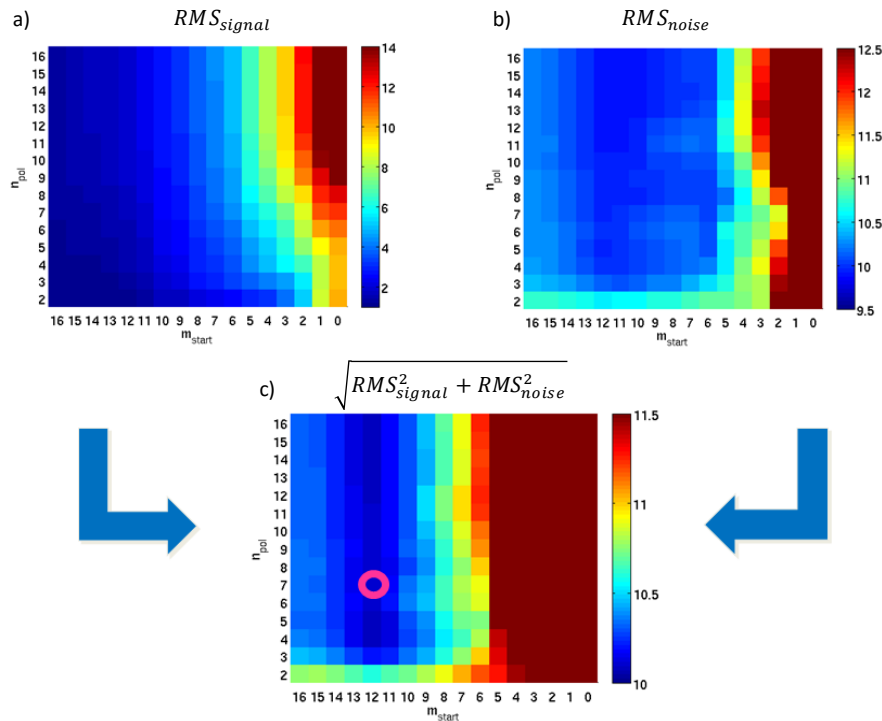


Figure 4. Effect of Swenson filter parameters m_{start} and n_{pol} on a) signal corruption, b) noise reduction and c) combined effect on signal and noise. RMS residuals are shown for the gravity field rates in (mm w.e./yr). The optimal choice of filter parameters $m_{start} = 12$ and $n_{pol} = 7$ is indicated as circle. Results are shown for GFZ RL05a with $j_{max} = 90$.

444 synthetic signal, RMS_{signal} . The RMS is evaluated in terms of water-equivalent height per year for the signal components within the region south of 60°S latitude.

For assessing the noise and noise reduction in the filtered fields, we face the task of
 447 separating the noise from the geophysical signals in the gravity field rates derived from GRACE. Here we attempt such a separation by reducing *a priori* information on the rate of ice mass change from the GRACE fields and considering the residual as an upper bound
 450 representation of noise. The *a priori* information is, again, based on elevation rates. For the



noise assessment we then take the RMS of the residual rates in terms of water equivalent height per year, RMS_{noise} , again for the region south of 60°S latitude. Since the residual gravity field rates may still contain some geophysical signal, we consider this noise estimate as an upper bound for the true GRACE uncertainties. It should be stated that, after the Swenson filtering, an additional Gaussian filtering is applied to the signal and noise models with a 200 km filter width, which was determined to be the optimal smoothing half-width for the signal-to-noise ratio in the GRACE spectra by Wiener optimal filtering (Sasgen et al. 2006) as reflected in the degree-amplitude spectrum.

Fig. 4 shows the assessed signal corruption and noise reduction as a function of the two Swenson filter parameter choices, the polynomial degree n_{pol} and the minimum order m_{start} . The results are shown for the gravity field expanded to degree and order $j_{max} = 90$ of the GFZ RL05a coefficients, even though using $j_{max} = 50$ and CSR RL05 yields similar results. As expected, the signal corruption, RMS_{signal} increases with increasing strength of the Swenson filter, that is with increasing n_{pol} and the decreasing minimum order m_{start} . In terms of noise reduction, we see as expected that stronger filtering (increasing n_{pol} ; decreasing m_{start}) decreases the RMS_{noise} (Fig. 4), however, only for the range of filter parameters with $m_{start} \geq 10$. For $m_{start} < 10$ this pattern is reversed. A closer analysis indicates that the consideration of the low orders into the Swenson filtering transfers energy (both from signal and noise) from low-to-mid latitudes to the Polar Regions. This leads to a considerable signal corruption that is only avoided by limiting the range of filter parameters in this regional analysis.

To define the optimal filter parameters a quadratic sum of the signal corruption and noise reduction is computed, allowing us to balance both effects, the optimal values are $m_{start} = 12$ and $n_{pol} = 7$ as indicated in Fig. 4c. These filter parameters are subsequently used. For



474 comparison it is stated that Chambers & Bonin, 2012 find $m_{start} = 15$ and $n_{pol} = 4$ as
optimal for oceanic applications.

4.2 Reduction of interannual mass variations

477 Interannual variations are a major constituent of the temporal variations of the Antarctic
gravity field (Wouters et al. 2014). A large portion of the non-linear signal in geodetic mass and
volume time series is well explained by modelled SMB fluctuations (Sasgen et al. 2010;
480 Horwath et al. 2012). Towards the ultimate goal of isolating the linear GIA signal from time
series of mass change, we removed non-linear effects of modelled SMB variations from the
GRACE time series; for this we calculate the *monthly cumulative SMB anomalies* with respect
483 to the time period 1979 to 2012 obtained from RACMO2/ANT (Lenaerts et al. 2012).

We then transfer the monthly cumulative SMB anomalies in terms of their water-equivalent
height change into the spherical harmonic domain and subtract them from the monthly GRACE
486 coefficients. In principle, the reduction of the SMB variations from the GRACE time interval
has two effects: first, it may change the overall gravity field rate derived from GRACE,
depending on the assumption of the SMB reference period. Ideally, the reference period reflects
489 a state of the ice sheet in which input by SMB equals the outflow by ice discharge, and SMB
anomalies estimated for today reflect the SMB component of the mass imbalance. However,
any bias in the SMB in the reference period leads to an artificial trend in the ice sheet mass
492 balance attributed to SMB. This is an undesired effect, and to avoid it we de-trend the
cumulative SMB time series for the time interval coeval to the GRACE analysis (February 2003
to October 2009), before subtracting it from the gravity field rates derived from GRACE (zero
495 difference for *Step 2*, Fig. 3). The second effect is the reduction of the post-fit RMS residual for
this known temporal signal variation. After reducing the SMB variations, the propagated RMS



uncertainty of the derived gravity field rate becomes closer to the uncertainty level of the
498 GRACE monthly solutions (Fig. 3).

4.3 Month-dependent weighting

The quality of GRACE monthly solutions changes with time, for example due to changing
501 orbital sampling patterns (Swenson & Wahr 2006). Fig. 5 shows the temporal evolution of RMS

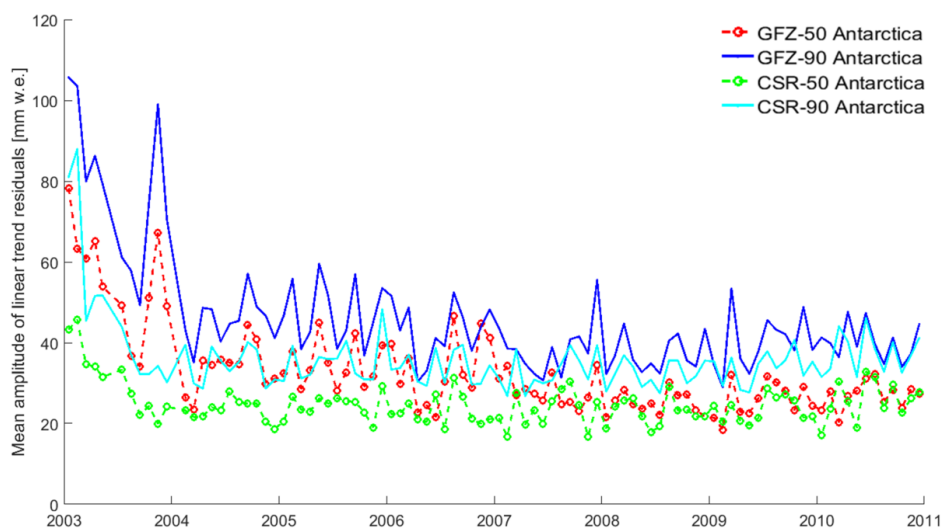


Figure 5. RMS uncertainty of monthly GRACE gravity fields for 2003-2011, averaged over the Antarctic region south of -60°S latitude. Shown are results for GFZ RL05a and CSR RL05 and $j_{max} = 50$ and $j_{max} = 90$.

uncertainties of the monthly GRACE gravity fields in the Antarctic region. Shown are residual
mass anomalies, integrated over Antarctica, after the grid-based removal of the temporal linear
504 trend and annual oscillation components and applying the filtering described in *Step 1*. To
improve the accuracy of the estimate of the gravity field rate, we include monthly uncertainties



as weights in our least-squares linear regression. Fig. 5 shows that these uncertainties are higher
507 during early 2003. Applying the monthly dependent weighting has the effect of reducing the
influence of the first months of the year 2003 on the estimated gravity field rate, which is similar
to shortening the time series, given the relatively large uncertainties. Also, the post-fit RMS
510 uncertainty associated with the rate reduces, if the early months of the year 2003 are excluded,
indicating that down-weighting the months from early 2003 is more beneficial than retaining a
longer time series. Altogether, the month-dependent weighting reduces the magnitude of stripe
513 patterns characteristic for the uncertainty of GRACE monthly solutions, and yields a more
accurate representation of propagated RMS uncertainty associated with the gravity field rates
(Fig. 3).



516 4.4 Gravity field rate and uncertainty assessment

Fig. 6 shows the estimated RMS uncertainty of the gravity field rate over Antarctica, after post-processing. It is evident that the largest uncertainties are located in a ring south of -80°S latitude. This is explained by the design of the Swenson filter; little or no noise reduction is
519 achieved close to the poles, as the gravity field is represented by near-zonal coefficients, which

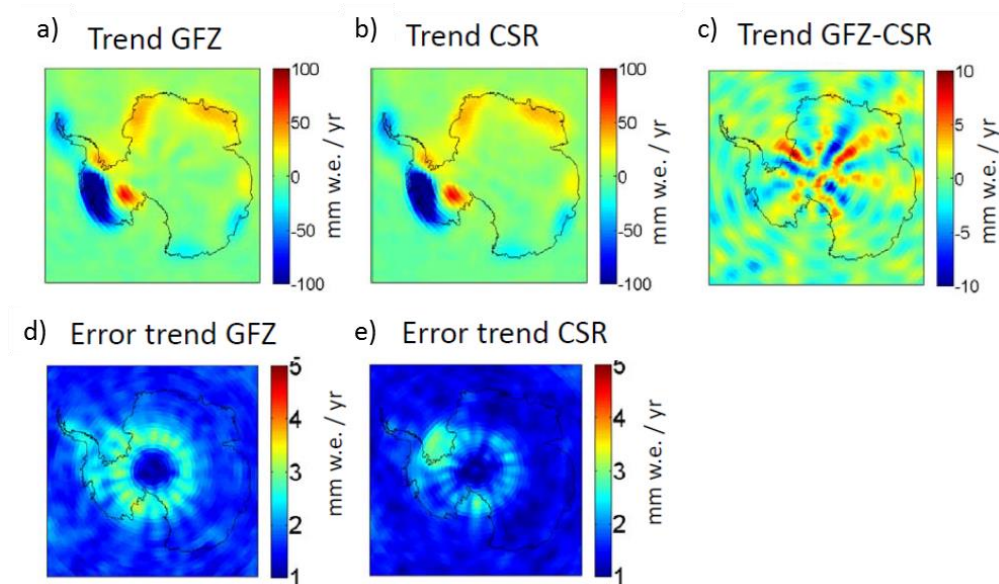


Figure 6. Linear trend in the GRACE gravity fields for the years 2003-2009; a) GFZ RL05a, b) CSR RL05, c) difference between rates from GFZ RL05 and CSR RL05, propagated d) RMS uncertainty for GFZ RL05a and e) RMS uncertainty for CSR RL05.

pass the filter mostly unchanged ($m_{start} = 12$). It is observed that extending the kernel of the
522 Swenson filter to these near-zonal coefficients ($m_{start} \leq 10$) creates high signal corruption
and is not suitable for the optimal rate estimate over Antarctica (see Section 4.1). Larger
uncertainties are also estimated for the Ronne and Ross ice shelf areas, which are most likely a
525 consequence of incomplete removal of the ocean tide signal during the GRACE de-aliasing



procedure (Dobslaw et al. 2013). It should also be stated that the RMS uncertainty estimate does not include possible systematic errors in the GRACE solutions, e.g. due to a long-term drift behavior of the observing system.

4.5 Selection of GRACE release

Our evaluation of the monthly GRACE uncertainties (Fig. 5), as well as the propagated RMS uncertainty of the temporal linear trend (Fig. 6) indicates that the lowest noise level for the Antarctic gravity field rate (February 2003 to October 2009) is currently achieved with GRACE coefficients of CSR RL05, expanded $j_{max} = 50$. We therefore refrain from including coefficients with $j_{max} > 50$ in order not to comprise the rate estimates by unnecessarily increasing the noise level (see Appendix A.5, Fig. A.3). We adopt CSR RL05 with $j_{max} = 50$ as our preferred solutions for the representation of the gravity field rates over Antarctica, even though GFZ RL05 with $j_{max} = 50$ yields very similar rates (Fig. 6). This choice is supported by the joint inversion, as CSR RL05 with $j_{max} = 50$ provides the highest level of consistency (lowest residual misfit) with the altimetry and GPS data sets (see REGINA Part II, Sasgen et al. 2013, Supplementary Information, Section S.3), which we interpret as minimum of spurious signals in the trends. To account for the uncertainty related to our choice of the solution, we consider not only RMS uncertainties of the GRACE rates but also solution differences, in the uncertainty of the final GIA estimate (Fig. 6). The solution difference represent the absolute deviation between trends from GFZ RL05 and CSR RL05 (February 2003 to October 2009, cut-off degree $j_{max} = 50$). These are then summed up squared with the propagated RMS uncertainties. It is acknowledged that the solution differences contain systematic noise arising from the GRACE processing; the pattern and magnitude may change over time. However, they provide a measure how much the results will change, if a GRACE release alternative to CSR



549 RL05 is considered. The difference between GRACE rates filtered with Gaussian smoothing of
200 km and the optimized Swenson filter together with Gaussian smoothing of 200 km is shown
in the Appendix A.5, Fig. A.4.

552 4.6 Data availability

4.6.1 Stokes coefficients of gravity field change

The monthly GRACE gravity field solutions from the Data System Centers GFZ and CSR
555 are available under <ftp://podaac.jpl.nasa.gov/allData/grace/L2/> or <http://isdc.gfz-potsdam.de/> as
spherical harmonic (SH) expansion coefficients of the gravitations potential (Stokes
confidents). More information is available in Bettadpur (2012). The data archive contains
558 temporal linear trends of the fully normalized Stokes coefficients in the ‘geodetic norm’
(Heiskanen & Moritz, 1967), complete to degree and order 90, inferred from these time series
according to Section 4,. We provide data for GFZ RL05 and CSR RL05, for the time period
561 2003-2009 and 2003-2013, and for various combinations of filtering. The coefficients are
organized as:

[Degree j], [Order m], [c_{jm}], [s_{jm}]

564 4.6.2 Code for de-stripping filtering

The Matlab® function “KFF_filt” performs decorrelation filtering for sets of spherical
harmonic coefficients, typically from GRACE gravity field solutions, after the idea of Swenson
& Wahr (2006). An open-source alternative to Matlab® is GNU Octave
567 <https://www.gnu.org/software/octave/>. The function is called as `KFF_filt =`
`swenson_filter_2(KFF, ord_min, deg_poly, factorvec, maxdeg)`, where variables `ord_min` and
570 `deg_poly` equal m_{start} and n_{pol} , respectively, in Section 4. KFF contains the sets of spherical
harmonic coefficients in the ‘triangular’ format (not memory-efficient but intuitive). For



example, for a set of coefficients with maximum degree $j_{\max} = 3$ and maximum order $m_{\max} =$

573 3, the set of coefficients is stored in a $j_{\max} \times m_{\max}$ matrix in the following way:

```
% KFF = [0  0  0  c_00 0  0  0;  
%      0  0  s_11 c_10 c_11 0  0;  
576 %      0  s_22 s_21 c_20 c_21 c_22 0;  
%      s_33 s_32 s_31 c_30 c_31 c_32 c_33]
```

579 5. VISCOELASTIC MODELLING

The Earth structure of Antarctica is characterized by a strong dichotomy between east and west, separated along the Transantarctic Mountains (e.g. Morelli & Danesi, 2004). Recent
582 seismic studies have produced refined maps of crustal thicknesses also showing slower upper-mantle seismic velocities in West Antarctica, indicating a thin elastic lithosphere and reduced mantle viscosity (An et al. 2015; Heeszel et al. 2016). Moreover, yield strength envelopes of
585 the Earth's crust and mantle suggest the possibility of a viscously deforming layer (DL) in the lower part of the crustal lithosphere (Ranalli & Murphy, 1987), a few tens of km thick and with viscosities as low as 10^{17} Pa s (Schotman et al., 2008). High geothermal heat flux is in
588 agreement with the seismic inferences of a thin elastic lithosphere and low mantle viscosity, and would favor the presence of such a DL also in West Antarctica (Shapiro & Ritzwoller 2004; Schroeder et al. 2014).

591 The choice of the viscoelastic modelling approach used to determine load-induced surface displacements and gravitational perturbations is governed by three main requirements; i) to accommodate a lateral variations in Earth viscosity, ii) to allow for Earth structures with thin
594 elastic lithosphere and low viscosity layers, in particular including a DL, and iii) to provide



viscoelastic response functions for the joint inversion of the satellite data described in REGINA
paper II (Sasgen et al. *submitted*). To meet these requirements, we adopt the time-domain
597 approach (Martinec 2000) for calculating viscoelastic response functions of a Maxwell
continuum to the forcing exerted by normalized disc-loads of constant radius. Then, the
magnitudes and spatial distribution of the surface loads are adjusted according to the satellite
600 data to obtain the full GIA signal for Antarctica. The forward modelling of viscoelastic response
functions a classic topic in solid Earth modelling (e.g. Peltier & Andrews, 1976), however, their
application to inverting multiple-satellite observations for present and past ice sheet mass
603 changes is new and applicable to other regions, such as Greenland or Alaska.

The viscoelastic response function approach allows for high spatial resolution at low
computational cost in the numerical discretization of the Earth structure as well as in the
606 representation of the load and the response. In addition, we can accommodate a high temporal
resolution, which is required when considering low viscosities and associated relaxation times
of only a few decades. The spherical harmonic cut-off degree for the simulations shown in the
609 following is $j_{max} = 2048$ (ca. 10 km).

5.1 Load model parameters

The load function $\sigma(t, \vartheta)$ is disc shaped with a constant radius of ca. 63 km. The radius of
612 63 km matches the mean radius of the discs south of 60°S of the geodesic grid (here, ICON 1.2
grid, status 2007, e.g. Wan et al., 2013), which underlie the joint inversion of the altimetry,
gravimetry and GPS observations (see REGINA paper II, Sasgen et al. *submitted*). The
615 resolution of the geodesic grid is chosen to allow for an adequate representation of the load and
viscoelastic response with regard to the input data sets, while minimizing the computational
cost. The disc load experiment consists of a linear increase in the ice thickness at a rate of 0.5



618 m/yr continuing until a new dynamic equilibrium state between load and response is reached.

With reference to the assumed ice density of 910 kg/m^3 , this thickness increase corresponds to a mass gain of *ca.* 5.6 Gt/yr . Then, to obtain the signal component of the viscous Earth response
621 only, the elastic response and the direct gravitational attraction of the load are subtracted.

The experiment is designed as an *increasing* load, for example representative for the ceasing motion of the Kamb Ice Stream (Ice Stream C; Retzlaff & Bentley, 1993), West
624 Antarctica. Due to linearity of the viscoelastic field equations, it is not necessary to calculate separately the equivalent *unloading* experiment, $-\sigma(t, \vartheta)$, for example corresponding to the past and present glacier retreat of the Amundsen Sea Sector, West Antarctica (Bentley et al.
627 2014 and Rignot et al. 2014, respectively). Among others, the combined inversion of the altimetry, gravity and GPS data (REGINA paper II, Sasgen et al. *submitted.*) solves for the magnitude and the sign of the load, allowing for ice advance as well as ice retreat.

630 5.2 Earth model parameters

We set up an ensemble of 58 simulations representing different parameterizations of the viscosity structure (Table 5), split into West Antarctica (56 simulations) and East Antarctica (2
633 simulations). For West Antarctica, varied parameters are the lithosphere thickness, h_L (30 to 90 km in steps of 10 km), the asthenosphere viscosity ($1 \times 10^{18} \text{ Pa s}$ to $3 \times 10^{19} \text{ Pa s}$ in four steps), and the presence of a ductile lower crust, DL, with 10^{18} Pa s . For East Antarctica, we
636 employ parameter combinations appropriate for its cratonic origin with h_L of 150 km and 200 km, and an asthenosphere viscosity equivalent to the upper-mantle viscosity of $5 \times 10^{20} \text{ Pa s}$. These values lie in the range of previously applied viscosity values in Antarctica (Nield et al.
639 2012; Whitehouse et al., 2012; Ivins et al., 2013; van der Wal et al., 2015). For the radial layering of the elastic properties, we adopt the Preliminary Reference Earth Model (PREM;



Dziewonski & Anderson 1981).

Table 5. Earth model parameters associated with the disc load ensemble simulations. The viscoelastic parameterization of the Earth model is discretized in six radial layers; upper and lower crust, mantle lithosphere, asthenosphere, upper and lower mantle. The lower mantle extends down to the core mantle boundary (CMB; at the depth of 2763 km). Elastic layers are represented by a quasi-infinite viscosity of 10^{30} Pa s.

Layer	Depth (km)	Viscosity (Pa s)	Unique param. val.
West Antarctica			
Upper crust	20	10^{30}	1
Lower crust DL [yes/no]	30	$[10^{30}/10^{18}]$	2
Mantle lithosphere	[30, 90, steps of 10]	10^{30}	7
Asthenosphere	200	$[1 \times 10^{18}, 3 \times 10^{18}, 1 \times 10^{19}, 3 \times 10^{19}]$	4
Upper mantle	670	5×10^{20}	1
Lower mantle	CMB	2×10^{22}	1
Number of simulations West Antarctica			56
East Antarctica			
Crust	30	10^{30}	1
Mantle lithosphere	[150, 200]	10^{30}	2
Upper mantle	670	5×10^{20}	1
Lower mantle to CMB	CMB	2×10^{22}	1
Number of simulations East Antarctica			2
Elastic earth			
Crust and mantle to CMB	CMB	10^{30}	1
Total number of simulations			59

642 Later, in the joint inversion, the distribution of viscoelastic response functions is based on
 the Earth structure model of Priestley & McKenzie (2013). Priestley & McKenzie (2013)
 provide a global distribution of viscosity values up to a depth of 400 km, which is sampled at
 645 the location of the geodesic grid. We then define a threshold value for the viscosity (here, 10^{22}
 Pas) above which the Earth response is considered purely elastic and infer the associated



thickness of the elastic lithosphere. Note that the Earth response in the equilibrium state only
648 depends on the lithosphere thickness (independent of viscosity), which is therefore consider as
the main Earth model parameters in the joint inversion. Further details are presented in
REGINA paper II, Sasgen et al. *submitted*.

651 5.3 Gravity and displacement rate response functions

The calculated response functions for surface deformation (radial displacement) and
gravity (geoid height change) are discretized along 1507 latitudinal points within the range $0 \leq$
654 $\vartheta \leq 90$. Simulations are typically run over 2 kyr with a temporal resolution of $\Delta t = 10$ yr (plus
two time steps with constant load thickness). For East Antarctic parameterizations, the
simulation period was extended to 20 kyr due to the higher upper-mantle viscosities and
657 associated slower relaxation. However, note that the ratio of geoid-height change versus radial
displacement falls off to $1/e$ after ca. 2 kyr of simulation (Appendix A.6, Fig. A.5). The forcing
expected in central East Antarctica is an increase in accumulation towards present-day
660 conditions after ca. 7 ka BP (van Ommen et al. 2004), justifying also the use of equilibrium
kernels for East Antarctica. The time derivatives of the radial displacement \dot{u} and of the geoid
height change \dot{e} are calculated with a central difference scheme.

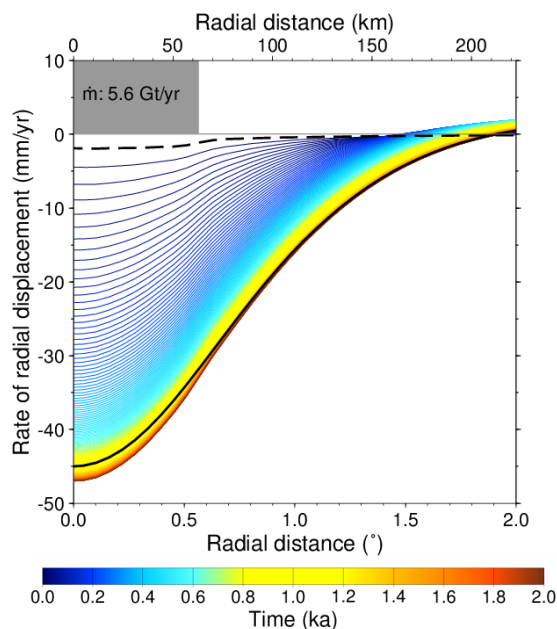


Figure 7. Displacement rates over the simulation period of 2 kyrs, for an exemplary set of Earth model parameters ($h_L = 30 \text{ km}$; $\eta_{AS} = 1 \times 10^{18} \text{ Pa s}$). Shown is the load dimension (grey shading), as well as the instantaneous elastic response (dashed black line) and viscoelastic relaxation only after 2 kyr and no load change (solid black line). The other curves show the rates for the time epoch indicated by the color scale.

663 Examples of response functions to the loading detailed in Section 5.1 for the rate of radial
displacement, \dot{u} , and rate of geoid-height change, \dot{e} , are shown in Figs 7 and 8, respectively.
Instantaneously, the increasing load, $\dot{\sigma}(t) = \text{const.}$, induces an elastic response that is
666 characterized by subsidence and an increase in the direct gravitational potential (dashed lines
in Fig. 7 and Fig. 8, respectively). This is the elastic response function adopted in the joint
inversion. Note that the elastic response function will not differ between East and West
669 Antarctica, as it is entirely based on the distribution of densities and elastic parameters provided
by the PREM. As the load build-up continues, the instantaneous response is followed by the

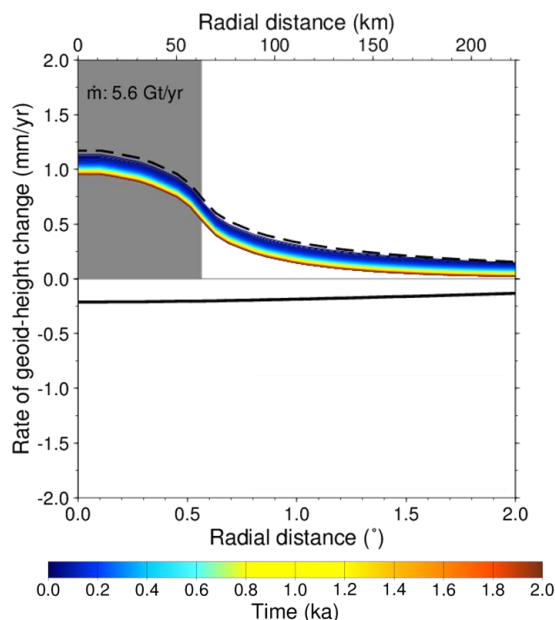


Figure 8. Same as Fig. 7, but for the rate of geoid-height change and Earth model parameters

$h_L = 90 \text{ km}$; $\eta_{AS} = 1 \times 10^{18} \text{ Pa s}$. Note the change in sign in the rate when the increase in direct gravitational attraction through load increase ceases after 2 kyr (black solid line vs. colored lines).

viscoelastic response, which depends in timing and magnitude on the underlying lithosphere
 672 and viscosity structure, further increasing the displacement rates, \dot{u} (blue to red lines in Fig. 7).
 The compensation by solid Earth deformation is reflected in the decreasing geoid rate, \dot{e} (Fig.
 8). After a certain time, which depends on the value of the asthenosphere viscosity, a new
 675 dynamic equilibrium state is reached at which \dot{u} and \dot{e} do not change in time any more. In the
 last two time steps, the load is kept constant ($\dot{\sigma}(t) = 0$), and the responses in \dot{u} and \dot{e} are only
 caused by the relaxation of the Earth's viscoelastic deformation (solid black line in Figs. 7 and
 678 8), which is the viscoelastic response function adopted in the joint inversion.



5.4 Discussion of effects of selected earth model parameterizations on GIA response

Fig. 9 shows the response of \dot{u} for four end-member sets of Earth model parameters with
681 thick lithosphere, weak asthenosphere (*TkWk*: $h_L = 90 \text{ km}$; $\eta_{AS} = 1 \times 10^{18} \text{ Pa s}$), thick
lithosphere, strong asthenosphere (*TkSg*: $h_L = 90 \text{ km}$; $\eta_{AS} = 3 \times 10^{19} \text{ Pa s}$), thin
lithosphere, weak asthenosphere (*TnWk*: $h_L = 30 \text{ km}$; $\eta_{AS} = 1 \times 10^{18} \text{ Pa s}$) and thick
684 lithosphere, strong asthenosphere (*TnSg*: $h_L = 30 \text{ km}$; $\eta_{AS} = 3 \times 10^{19} \text{ Pa s}$), without a
ductile layer, DL. In this context, thick / thin and strong / weak refer to values in comparison to
the ‘average’ value of the ensemble for West Antarctica; an elastic lithosphere of thickness 90
687 km (here, ‘*Tk*’) is in the range of global average continental lithosphere usually applied in GIA
studies (e.g. Peltier, 2004), or that of East Antarctica (150 to 200 km). Fig. 10 shows the
response in \dot{u} for the same end-member set of Earth model parameters with a DL included. It
690 should be stated that the Earth structure with $h_L = 30 \text{ km}$ and a DL is considered very extreme,
because in this case the ductile layer extends down to the asthenosphere and an elastic mantle
lithosphere is missing.

693 Fig. 9 and 10 show that for the weak asthenosphere ($\eta_{AS} = 1 \times 10^{18} \text{ Pa s}$), viscoelastic
deformation is visible already after one decade of loading (or unloading), leading to
considerably larger subsidence rates compared to the purely elastic case even on very short time
696 scales. For these Earth model parameters, a new dynamic equilibrium state is achieved within
a few centuries. The rates of subsidence in this equilibrium then primarily depend on the support
provided by the flexure of the elastic lithosphere.

699 For the extreme *TnWk* case, equilibrium rates of -45 mm/yr are achieved at the load
centre, and considerable subsidence of -20 mm/yr already occurs after ten years of loading
(Fig. 9). Increase in asthenosphere viscosity (*TnSg* case) reduces the viscous material transport



702 and leads to a slower adjustment towards the dynamic equilibrium state, which takes more than
 1 kyr. It should be stated that in our definition of the ensemble parameters, reducing the

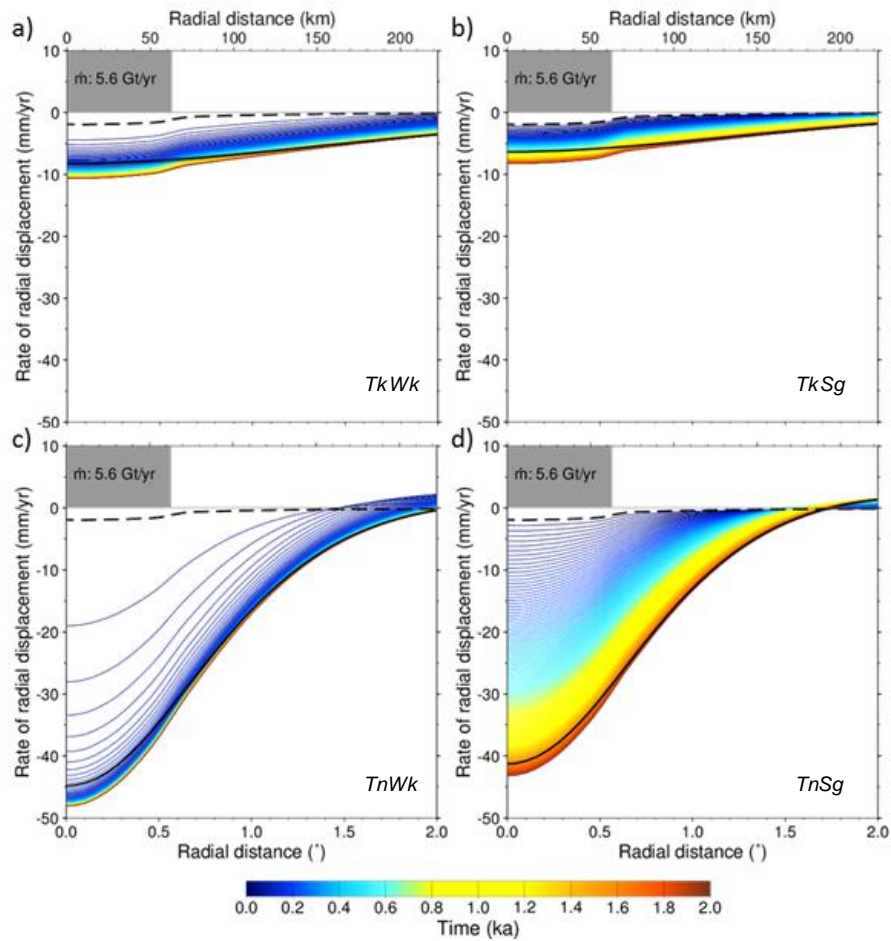


Figure 9. Same as Figure 7, but for four end-member sets of Earth model parameters, without a
 DL and lithosphere thickness / asthenosphere viscosity of a) $h_L = 90 \text{ km} / \eta_{AS} = 1 \times 10^{18} \text{ Pa s}$ (TkWk), b) $h_L = 90 \text{ km} / \eta_{AS} = 3 \times 10^{19} \text{ Pa s}$ (TkSg), c) $h_L = 30 \text{ km} / \eta_{AS} = 1 \times 10^{18} \text{ Pa s}$ (TnWk) and d) $h_L = 30 \text{ km} / \eta_{AS} = 3 \times 10^{19} \text{ Pa s}$ (TnSg).



lithosphere thickness in turn increases the thickness of the asthenosphere (bottom depth of
 705 asthenosphere is fixed), which facilitates lateral material transport inside the asthenosphere.

The consideration of the DL in the Earth structure causes a thinning of the effective elastic

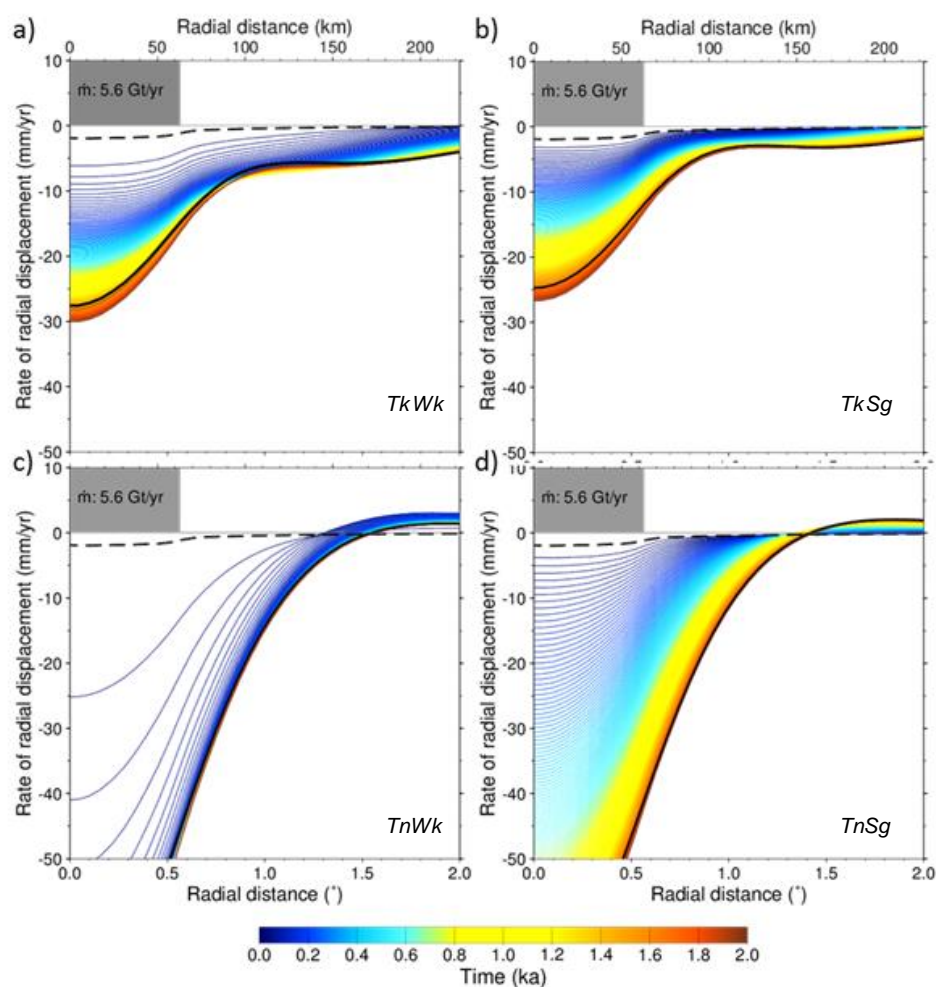


Figure 10. Same as Figure 9, a) *TkWk*, b) *TkSg* (b), *TnWk* (c) and *TnSg* (d), but with the Earth structure including a DL.

lithosphere. As a consequence, greater and more localized subsidence rates are produced for all
 708 sets of parameters (Fig. 10). Interestingly, in case of a thick elastic lithosphere (90 km), the



radial displacement exhibits a local minimum at around 120 and 160 km distance from the load centre (Fig. 10), which is a consequence of the viscous material transport inside the ductile layer. The maximum equilibrium rate of -76 mm/yr is achieved for the *ThWk* case with DL, where the viscous deformation leads to rates of -25 mm/yr already after 10 yrs of loading.

5.5 Assumptions and limitations

Although the approach of modelling response functions to axisymmetric disc loads and subsequently superposing them is very efficient in terms of the computational cost, this simplification introduces some limitations. First, the superposition of response functions representing different Earth structures neglects the transmission of stresses between these regions — a problem that can only be resolved with fully three-dimensional solid Earth modelling (e.g. van der Wal et al., 2015). The largest impact for the displacement rates is expected in regions with lateral contrasts in lithosphere thickness and mantle viscosity such as the Transantarctic Mountains. Second, the constant disc radius of about 63 km implies that finer-scale deformation cannot be resolved. Although this resolution is adequate for interpreting GRACE data (spatial half-wavelength of *ca.* 200 km) smaller-scale loading excitement may be necessary for interpreting local GPS measurements near to the loading, particularly for the elastic response to present-day glacial changes.

5.6 Data availability

5.6.1 Viscoelastic kernels

Output files contain 1507 latitudinal points ($0 \leq \vartheta \leq 90$) covering a region greater than the size of the Antarctic domain, as well 203 time steps of West Antarctica (213 time steps for East Antarctica, because of extending the simulation period to 15 kyrs). The time derivative of the



radial displacement, u , is calculated with a central difference scheme, $y^u := [u(t+\Delta t/2)-u(t-$
 732 $\Delta t/2)]/\Delta t$. The difference between two time steps is $\Delta t=10$ yr. The same applies to the rate of
 geoid-height change, y^g . Note that the load is constant during the last two time steps (no rate
 of change); therefore, the kernels represent the viscoelastic relaxations only, without the
 735 instantaneous elastic deformation or the direct gravitational attraction of the load.

The results are stored independently for the rheology of East and West Antarctica, the latter
 with and without a ductile layer in the elastic part of the lithosphere. The data are stored in a
 738 Matlab® file format, which is also readable with GNU Octave
<https://www.gnu.org/software/octave/>.

- ‘Viscoel_response_WA_with_DL.mat’ – Response functions for West Antarctica
 741 *with* ductile layer
- ‘Viscoel_response_WA_no_DL.mat’ – Response functions for West Antarctica
without ductile layer
- 744 • ‘Viscoel_response_EA_no_DL.mat’ – Response functions for East Antarctica
without ductile layer
- ‘Time_EA_rheo.mat / Time_WA_rheo.mat’ – Time [kyr] file related to response
 747 file for East and West Antarctica
- ‘Coord_Co-Latitude.mat’ – Co-latitude [°] of the response functions

The response matrix summary the data as follows:

750 *West Antarctica:*

VE_WA_no_DL has the following entries, [HL, AV, LAT, TIME, VAR]

HL: Lithosphere thickness; 30 km, 40 km, ..., 90 km (7 entries)

753 AV : Asthenosphere Viscosity; 1×10^{18} Pa s, 3×10^{18} Pa s, 10×10^{18} Pa s, $30 \times$



10^{18} Pa s (4 entries)

LAT: Latitude grid node, corresponding to file ‘Coord_Co-Latitude.mat’ (1537 entries)

756 TIME: Time, corresponding to file ‘Time_WA_rheo.mat’ (202 entries)

VAR: Variable type; 1: rate of radial displacement in mm/yr, 2: rate of geoid-height change in mm/yr.

759 The response kernels for *East Antarctica* are organized analogue, [HL, LAT, TIME, VAR]

HL: Lithosphere thickness; 150 km, 200 km (2 entries)

Note that the asthenosphere and upper mantle viscosity is constant at $5 \times 10^{20} \text{ Pa s}$ and

762 therefore has no entry.

The spectral resolution underlying these fields is spherical-harmonic cut-off degree 2048.

The user should apply an adequate smoothing filter when using for inverting GRACE gravity

765 fields. Filtered kernels are available upon request by the author.

5.6.2 Geodesic grid

The computation of the geodesic grid is not an original contribution of the authors, but
768 based on the grid generator of the ICON GCM project, <http://icon-downloads.zmaw.de/>. For completeness, we provide the data set with disc locations based. An alternative resource for downloading geodesic grids at different resolutions in netCDF format can be found here:

771 <http://kiwi.atmos.colostate.edu/BUGS/geodesic/> .

The files format is:

vert-7.mask.cont_and_shelf.re.dat: Longitude [°], Latitude [°]

774 vert-7.mask.cont_and_shelf.re.proj.dat: X [km], Y [km], (projected coordinates, WGS-84, Polar Stereographic, 71°S true latitude, 0°E central longitude)



777

5.6.3 *Lithosphere thickness*

The thickness of the elastic lithosphere at the locations of the geodesic grid for different
780 values of the viscosity threshold applied to the data set of Priestley & McKenzie, 2013.

lith_thresh_21.disc.txt (threshold 10^{21} Pa s, thicker lithosphere)

lith_thresh_22.disc.txt (threshold 10^{22} Pa s, lithosphere adopted in the GIA estimate)

783 lith_thresh_23.disc.txt (threshold 10^{23} Pa s, thinner lithosphere)

The 1175 entries correspond to the locations of the geodesic grid (Section 5.6.2).

5.6.4 *Open source code for viscoelastic modelling*

786 The opens source software package SELEN allows the computation of the Maxwell-
viscoelastic Earth response to user-defined ice sheet evolutions, in particular also a simplified
disc-load forcing as presented in this paper. The program is downloadable at:

789 <https://geodynamics.org/cig/software/selen/>

6. CONCLUSIONS

In this paper, we have presented refined temporal linear trends of surface elevation, gravity
792 field change and bedrock displacement based on Envisat/ICESat (2003-2009), GRACE (2003-
2009) and GPS (1995-2013.7), respectively. In addition, we have performed forward modelling
of the viscoelastic response of the solid Earth to a disc-load forcing. These response functions
795 are particularly suited to represent the distinct geological regimes of East and West Antarctica
in the joint inversion of multiple satellite data. Similarly, the functions can be applied to the
other geographical regions as well. The data and code necessary to reproduce our results, or
798 apply our approach to a different problem, is provide at www.pangea.de,
<https://doi.pangea.de/10.1594/PANGAEA.875745>.



We have refined surface-elevation rates for the Antarctic ice sheet for the time interval
801 2003-2009 by combining Envisat and ICESat altimetry data. The straightforward compositing
approach performs a grid-based comparison of the noise in the elevation rates obtained from
Envisat and ICESat. For large parts of the ice sheet, the elevation rate is based on ICESat data,
804 particularly, along for the rough terrain along coast, as well as close to the Pole (polar gap of
Envisat). Envisat contributes in some low-relief areas in East Antarctica and along the Antarctic
Peninsula, as well as along single spurious ICESat tracks. Thus, the composite elevation rates
807 are maximized in terms of spatial coverage and minimized in term of uncertainties.

The GPS processing carried out as part of the RATES and REGINA projects has produced
a comprehensive data set of Antarctic 118 GPS records, which, for continuous sites,
810 spans a longer time interval (1995-2013) than those of previous studies (Thomas et al.
(2011), 1995-2011; Argus et al. (2014), 1994-2012; Martín-Español et al. (2016b), 2009-
2014). The ensemble processing done for the REGINA project has allowed us to assess the
813 contribution of systematic error sources. In addition, for sites where there is potential doubt
over the quality of the metadata or the behaviour of the site, we have adopted a ‘conservative
but realistic’ approach to assigning new confidence limits. The screening of GPS data for
816 outliers involved careful manual assessment, encompassing the review of measurement logs
and notes on problems in the field. The data quality is reflected in the uncertainty estimates for
the GPS rates, which therefore represents more reliable input data than GPS rates based on
819 processing without manual intervention.

We have optimized the post-processing sequence for estimating the temporal linear trend
and its uncertainty in the GRACE gravity field solutions for the region of Antarctica. In
822 particular, we have derived optimal parameters for de-stripping the monthly gravity fields over



Antarctica according to Swenson & Wahr (2006). In addition, we have removed de-trended
interannual SMB fluctuation from the GRACE time series, to obtain a more representative
825 uncertainty estimate based on the post-fit RMS residual. We have included month-dependent
weighting in the least-squares estimate of the gravity field rates to account for the varying
quality of the monthly GRACE solutions. The optimization of the de-correlation filter of
828 Swenson & Wahr (2006) to the signals expected in Antarctica reduced the residual uncertainty
and improved the reliability of inferred mass anomalies.

With the aim of joining the multiple satellite data using the knowledge of the geophysical
831 processes involved, we have calculated elastic and viscoelastic response functions of the solid
Earth. The viscoelastic response functions represent the gravity field change and surface
displacement to a disc-load forcing for a variety of Earth model parameters; particularly,
834 however, values of mantle viscosity and lithosphere thickness strongly varying between the
distinct geological regimes of West and East Antarctica.

In particular, we have investigated the effect of a ductile layer in the crustal lithosphere on
837 the viscoelastic rebound signature. We show that for moderate load changes of 0.45 m/yr water-
equivalent (here, applied as disc load with a radius of ca. 63 km), uplift rates reach the cm/yr
level within decades assuming asthenosphere viscosities $< 10^{19}$ Pa s and lithosphere thickness
840 < 50 km; both plausible values for parts of West Antarctica. Including a ductile layer in the
crustal lithosphere further attenuates the uplift rates and localizes the deformational response.
This suggests that GIA in West Antarctica may locally be a result of more recent, centennial
843 load changes, most notably in the Amundsen Sea Embayment and in part of the Antarctic
Peninsula (Nield et al. 2012). Similar conclusion were reached by Ivins & James (2005) and
Nield et al. (2014).



846 The advantage of the viscoelastic response kernels is that a meaningful ratio of gravity
disturbance versus surface displacement is calculated for each choice of the Earth model
parameters, avoiding the approximation with an average rock density (e.g. Riva et al. 2009;
849 Gunter et al. 2014). Using the response functions allows us to reconcile GIA signatures with
measurements of large bedrock uplift and small gravity field increase in the Amundsen Sea
Embayment, associated with weak Earth structures. Clearly, the response functions adopted
852 here represent only the viscoelastic equilibrium state and, thus, are considered only an
intermediate step to full dynamic modelling of the GIA response. Nevertheless, this
approximation represents a significant improvement of other joint inversion methods, as it bases
855 the joint inversion on physically meaningful response kernels. With extra data on the past ice
evolution, such as Paleo thickness rates, our approach can be expanded to address the temporal
evolution as well.

858 In the succeeding paper REGINA part II (Sasgen et al. *submitted*), we perform the joint
inversion for present-day ice-mass changes and GIA in Antarctica, based on the input data sets
and viscoelastic response functions presented here. We validate our results using forward-
861 modelling results and other empirical models, and show the impact on CryoSat-2 volume and
GRACE mass balances, respectively. Note, however, that the post-processing methods and
viscoelastic functions presented here are applicable also to other geographical regions with
864 superimposed present-day mass change and GIA signatures.

7. DATA AVAILABILITY

The altimetry, gravimetry, GPS and viscoelastic modelling data used in this project are
867 available at <https://doi.pangaea.de/10.1594/PANGAEA.875745> in the www.pangea.de archive.
The data description and user documentation are given for each data type within the respective



subsection of this paper (Sections 2 to 5).

870 **AUTHOR CONTRIBUTION**

Ingo Sasgen conceived, managed and summarized this study with support of Mark R. Drinkwater. Alba Martín-Español, Bert Wouters and Jonathan L. Bamber performed the
873 altimetry analysis. Alexander Horvath, Martin Horvath and Roland Pail undertook the gravity field analysis, Elizabeth J. Petrie and Peter J. Clarke analysis and clustered the GPS data with critical input from Terry Wilson. Volker Klemann and Hannes Konrad performed the
876 viscoelastic modelling, with contributions from Ingo Sasgen. All authors were involved in writing and reviewing this manuscript.

COMPETING INTEREST

879 The authors declare that they have no conflict of interest.

ACKNOWLEDGEMENTS

The www.regina-science.eu work was enabled through CryoSat+ Cryosphere study
882 funding from the Support To Science Element (STSE) of the European Space Agency (ESA) Earth Observation Envelope Programme. I.S. acknowledges additional funding through the German Academic Exchange Services (DAAD) and DFG grant SA1734/4-1 and P.J.C. and
885 E.J.P. from UK NERC grant NE/I027401/1 (RATES project). We thank Thomas Flament and Frederique Rémy for the Envisat data and Veit Helm for providing the AWI L2 CryoSat-2 re-tracked and corrected elevation measurements. The GPS data used was mainly downloaded
888 from publically available archives. We acknowledge work done by the International GNSS Service (Dow et al., 2009), UNAVCO and the Scientific Committee on Antarctic Research in maintaining such archives, together with the efforts of all the GPS site operators in collecting



891 and making available the data, a particularly challenging task in Antarctica (see Table S2 for
more information on individual sources).



894

APPENDIX

A.1 ICESat campaigns and operation periods

Table A.1. ICESat 633 Level 2 data for the time span February 2003 until October 2009 used in this study.

Start Date	End Date	Days in Operation	Laser Identifier
20/02/2003	29/03/2003	38	1AB
25/09/2003	19/11/2003	55	2A
17/02/2004	21/03/2004	34	2B
18/05/2004	21/06/2004	35	2C
03/10/2004	08/11/2004	37	3A
17/02/2005	24/03/2005	36	3B
20/05/2005	23/06/2005	35	3C
21/10/2005	24/11/2005	35	3D
22/02/2006	28/03/2006	34	3E
24/05/2006	26/06/2006	33	3F
25/10/2006	27/11/2006	34	3G
12/03/2007	14/04/2007	34	3H
02/10/2007	05/11/2007	37	3I
17/02/2008	21/03/2008	34	3J
04/10/2008	19/10/2008	16	3K
25/11/2008	17/12/2008	23	2D
09/03/2009	11/04/2009	34	2E
30/09/2009	11/10/2009	12	2F

897



A.2 Firn compaction and SMB corrections

We apply rates of firn compaction, h_{comp} , using output of the firn compaction model
900 provided by Ligtenberg (2011), which is driven by RACMO2/ANT (Lenaerts 2010). However,

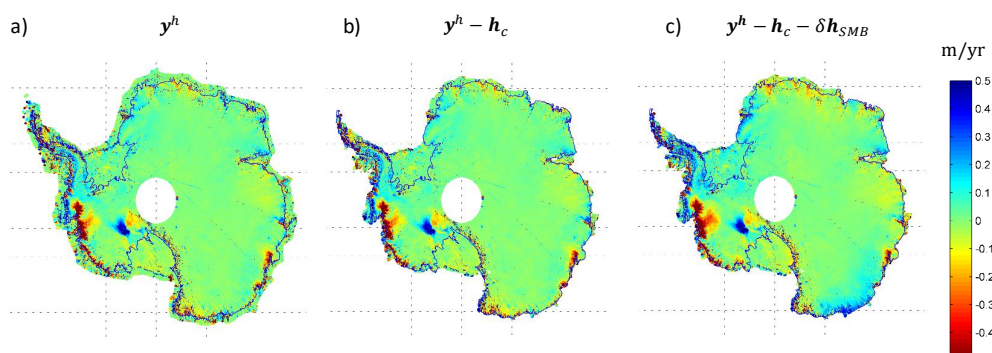


Figure A.1 Rate of elevation change y^h (m/yr), derived from a) ICESat/Envisat initial data, b) ICESat/Envisat minus firn compaction h_{comp} , and c) ICESat/Envisat minus firn compaction h_{comp} and modelled SMB anomalies δh_{SMB} .

we do not apply a correction for anomalies in the surface-mass balance (SMB), δh_{SMB} , as e.g. undertaken by Gunter et al. (2014), due to the problem of defining an adequate reference period
903 for the ice sheet. The impact of each correction is shown in Fig. A.1.



A.3 Flowchart of estimation process for Antarctic GPS site time series.

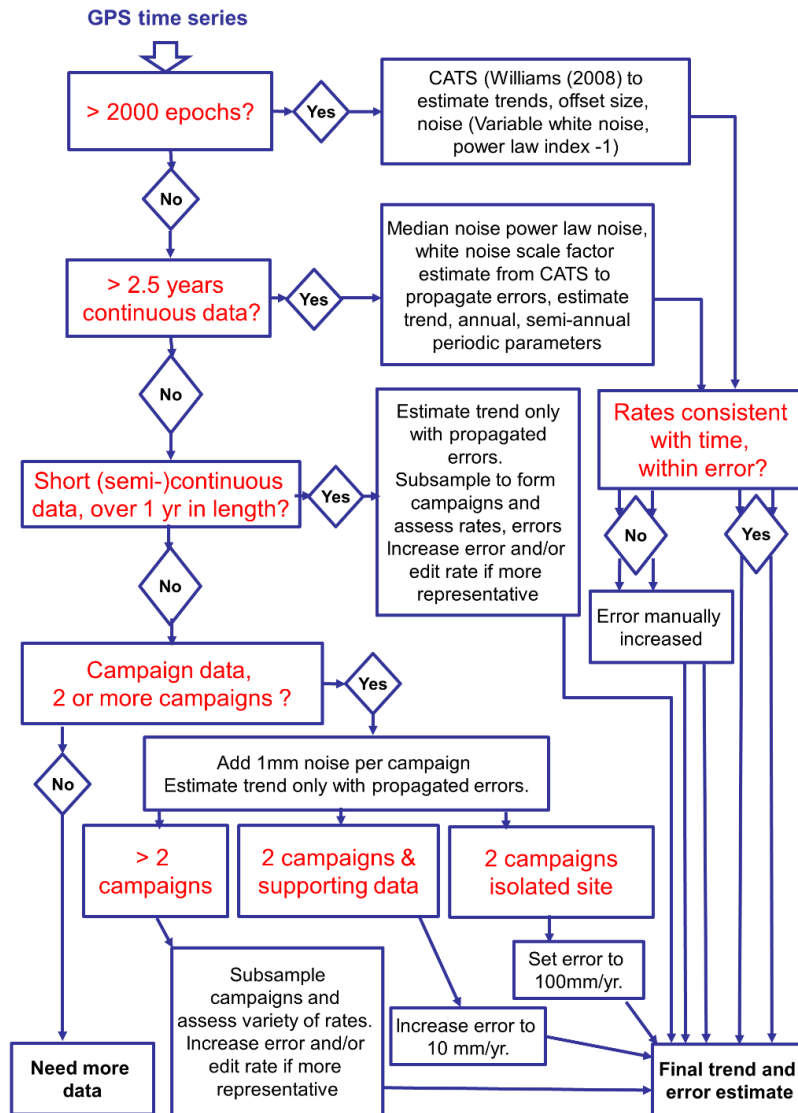


Figure A.2 Flowchart showing the estimation process for the temporal linear trends of the bedrock for Antarctic GPS site timeseries. After Petrie et al. (2016) (SCAR poster)



A.4 Uplift rates at all GPS site used in this study

Table A.2 GPS uplift rates for this study. The columns are: site name, estimated uplift rate y^u (mm/yr), estimated uncertainty σ^u (mm/yr), rate method, uncertainty method, approx latitude (dec. degrees), approx. longitude (dec. degrees). Methods are: cats: estimated by the CATS noise analysis software ('cats'), median uncertainty from CATS sites propagated ('prop'), manual intervention in rate due to potential systematic uncertainties ('rman') and manual intervention in uncertainties due to potential systematic errors ('eman').

Site name	y^u	σ^u	Method y^u	Method σ^u	Lat. (°)	Lon. (°)	Doi/ data source or description
aboa	0.6	0.5	cats	cats	-73.04	-13.41	Finnish Geodetic Institute
brip	1.4	0.7	cats	cats	-75.80	158.47	doi:10.7283/T5W09473
buri	2.3	0.7	cats	cats	-79.15	155.89	doi:10.7283/T5RB72W7
cas1	1.5	0.2	cats	cats	-66.28	110.52	IGS: Dow et al. (2009)
cote	1.4	0.7	cats	cats	-77.81	162.00	doi:10.7283/T5GT5KGN
crar	0.7	0.4	cats	cats	-77.85	166.67	UNAVCO*
dav1	-1.6	0.6	rman	eman	-68.58	77.97	IGS: Dow et al. (2009)
dum1	-0.3	0.3	cats	cats	-66.67	140.00	IGS: Dow et al. (2009)
flm5	2.0	0.6	cats	cats	-77.53	160.27	doi:10.7283/T5V40SH6
ftp4	1.9	0.6	cats	cats	-78.93	162.56	doi:10.7283/T5B27SKD
maw1	-0.4	0.2	cats	cats	-67.60	62.87	IGS: Dow et al. (2009)
mcm4	0.8	0.2	cats	cats	-77.84	166.67	IGS: Dow et al. (2009)
min0	2.0	0.8	cats	cats	-78.65	167.16	doi:10.7283/T5TM78BX
ohi2	3.4	2.0	cats	eman	-63.32	-57.90	IGS: Dow et al. (2009)
palm	4.8	3.0	cats	eman	-64.78	-64.05	IGS: Dow et al. (2009)
ramg	2.4	0.8	cats	cats	-84.34	178.05	doi:10.7283/T51N7ZFR
rob4	1.1	0.5	cats	cats	-77.03	163.19	doi:10.7283/T5NC5ZG8
sctb	0.9	0.5	cats	cats	-77.85	166.76	doi:10.7283/T5CF9N6P
syog	1.1	0.2	cats	cats	-69.01	39.58	IGS: Dow et al. (2009)
tnb1	0.1	0.5	cats	cats	-74.70	164.10	Dubbini et al. (2010)
vesl	0.4	0.3	cats	cats	-71.67	-2.84	IGS: Dow et al. (2009)
a351	-0.9	1.8	prop	eman	-72.91	74.91	Geoscience Australia**
a368	-0.2	1.2	prop	eman	-74.29	66.79	Geoscience Australia**
arct	-0.1	4.4	prop	eman	-80.04	-80.56	SCARP***
art1	-3.1	10.0	prop	eman	-62.18	-58.90	Dietrich et al. (2004)
back	16.8	5.0	prop	eman	-74.43	-102.48	doi:10.7283/T5D21VWM
bean	2.1	4.3	rman	eman	-75.96	-69.30	doi:10.7283/T55Q4T6R



belg	-1.4	0.7	prop	prop	-77.87	-34.63	Dietrich et al. (2004)
benn	9.3	1.9	prop	prop	-84.79	-116.46	doi:10.7283/T5891447
berp	25.2	0.7	prop	prop	-74.55	-111.88	doi:10.7283/T54J0CC2
bhil	2.9	4.4	rman	eman	-66.25	100.60	Geoscience Australia**
bren	3.1	1.1	rman	eman	-72.67	-63.03	doi:10.7283/T52V2D7X
capf	4.0	1.4	rman	eman	-66.01	-60.56	doi:10.7283/T5XP736P
cjam	-2.3	100.0	prop	eman	-63.10	-62.72	SCARP***
clrk	3.6	1.4	prop	prop	-77.34	-141.87	doi:10.7283/T5MK6B6C
coat	-0.1	7.3	prop	eman	-77.81	162.00	Raymond et al. (2004)
crdi	2.1	0.6	prop	prop	-82.86	-53.20	doi:10.7283/T5C24TQS
cwal	0.4	100.0	prop	eman	-63.25	-62.18	SCARP***
dal1	4.9	34.4	prop	eman	-62.24	-58.68	Dietrich et al. (2004)
dall	-17.0	100.0	prop	eman	-62.24	-58.66	Dietrich et al. (2004)
devi	1.9	1.0	prop	prop	-81.48	161.98	doi:10.7283/T5794Z20
dupt	11.5	1.1	prop	prop	-64.81	-62.82	doi:10.7283/T5KD1W62
eacf	-4.8	15.0	rman	eman	-62.08	-58.39	Brazil
elph	6.3	100.0	prop	eman	-61.22	-55.14	SCARP***
esp1	5.6	100.0	prop	eman	-63.40	-57.00	Dietrich et al. (2004)
fall	4.8	1.3	prop	prop	-85.31	-143.63	doi:10.7283/T53J3B84
ferr	-5.5	31.0	rman	eman	-62.09	-58.39	Dietrich et al. (2004)
fie0	-0.9	1.9	prop	prop	-76.14	168.42	doi:10.7283/T5KK993F
flm2	3.8	11.7	rman	eman	-77.53	160.27	doi:10.7283/T53T9FHJ
fonp	13.5	1.8	prop	prop	-65.25	-61.65	doi:10.7283/T5668B66
for1	-0.2	2.9	prop	eman	-70.78	11.83	Dietrich et al. (2004)
for2	-0.3	2.7	prop	eman	-70.77	11.84	Dietrich et al. (2004)
fos1	3.1	1.3	prop	eman	-71.31	-68.32	doi:10.7283/T54T6GF7
frei	-4.4	0.7	prop	prop	-62.19	-58.98	Bevis et al. (2009)
ftp1	-2.2	3.4	prop	eman	-78.93	162.56	doi:10.7283/T53T9FHJ
gmez	1.5	4.8	rman	eman	-73.89	-68.54	doi:10.7283/T58G8HT4
grw1	-7.0	8.6	prop	eman	-62.22	-58.96	Dietrich et al. (2004)
haa1	3.9	100.0	prop	eman	-77.04	-78.29	British Antarctic Survey
haag	6.1	1.1	rman	eman	-77.04	-78.29	doi:10.7283/T5FT8JB8
howe	0.6	1.1	rman	eman	-87.42	-149.43	doi:10.7283/T5ZW1J65
hown	3.9	0.8	prop	prop	-77.53	-86.77	doi:10.7283/T56971WH
hton	4.8	3.7	prop	eman	-74.08	-61.73	doi:10.7283/T5222RV6
hugo	0.9	1.3	prop	prop	-64.96	-65.67	doi:10.7283/T5FQ9TW3
iggy	2.3	1.1	prop	eman	-83.31	156.25	doi:10.7283/T5QC01T9
jnsn	4.0	1.7	prop	prop	-73.08	-66.10	doi:10.7283/T5S11HP1
lntk	4.6	3.1	rman	eman	-74.84	-73.90	doi:10.7283/T5J1017P
lply	2.0	8.1	rman	eman	-73.11	-90.30	doi:10.7283/T5DV1H50
lwn0	2.1	1.0	prop	prop	-81.35	152.73	doi:10.7283/T5T43RD8
mait	0.4	1.1	rman	eman	-70.77	11.74	Dietrich et al. (2004)
mar1	7.1	10.0	prop	eman	-64.24	-56.66	Dietrich et al. (2004)
mbl1	2.5	3.0	prop	eman	-78.03	-155.02	Donnellan & Luyendyk (2004) + doi:10.7283/T5CJ8BS7



mbl2	2.3	10.0	prop	eman	-76.32	-144.31	Donnellan & Luyendyk (2004)
mbl3	1.3	17.9	rman	eman	-77.34	-141.87	Donnellan & Luyendyk (2004)
mcar	3.7	1.4	prop	prop	-76.32	-144.30	doi:10.7283/T55D8Q41
mirn	24.4	100.0	prop	eman	-66.55	93.01	SCAR
mkib	4.7	2.6	rman	eman	-75.28	-65.60	doi:10.7283/T5D798HD
mtcx	-3.8	10.0	prop	eman	-78.52	162.53	Raymond et al. (2004)
ohg1	4.5	10.0	prop	eman	-63.32	-57.90	Dietrich et al. (2004)
ohig	4.0	0.7	prop	prop	-63.32	-57.90	Former IGS: Dow et al. (2009)
pal1	8.1	10.0	prop	eman	-64.77	-64.05	Dietrich et al. (2004)
patn	4.8	0.7	prop	prop	-78.03	-155.02	doi:10.7283/T5PC30PX
pece	0.7	4.2	prop	eman	-85.61	-68.56	doi:10.7283/T5930RG1
pra1	4.2	10.0	prop	eman	-62.48	-59.65	Dietrich et al. (2004)
prat	-9.6	100.0	prop	eman	-62.48	-59.65	doi:10.7283/T5M32T21 , doi:10.7283/T5K35RZP
prtt	-5.0	100.0	prop	eman	-62.48	-59.67	SCARP***
reyj	151.3	300.0	prop	eman	-62.20	-58.98	doi:10.7283/T5M32T21 , doi:10.7283/T5K35RZP , doi:10.7283/T5057D6V , doi:10.7283/T53T9FHJ
rob1	5.4	5.1	prop	eman	-77.03	163.19	doi:10.7283/T53T9FHJ
robi	8.7	1.5	prop	prop	-65.25	-59.44	Nield et al. (2014)
rot1	6.5	10.0	prop	eman	-67.57	-68.13	SCAR
rotb	5.0	0.4	prop	prop	-67.57	-68.13	doi:10.7283/T56M34Z7
roth	5.5	1.4	prop	prop	-67.57	-68.13	IGS: Dow et al. (2009)
sdly	-0.3	1.4	prop	prop	-77.14	-125.97	doi:10.7283/T5S46Q7F
sig1	23.0	100.0	prop	eman	-60.71	-45.59	Dietrich et al. (2004)
smr1	0.5	10.0	prop	eman	-68.13	-67.10	Dietrich et al. (2004)
smrt	1.2	0.9	prop	prop	-68.13	-67.10	Alfred Wegener Institute / Instituto Antartico Argentina
sppt	12.9	100.0	prop	eman	-64.29	-61.05	Bevis et al. (2009)
sugg	4.7	1.3	rman	eman	-75.28	-72.18	doi:10.7283/T5CV4G1M
svea	1.3	1.1	prop	prop	-74.58	-11.23	Sjoberg et al. (2011)
thur	-1.2	2.5	rman	eman	-72.53	-97.56	doi:10.7283/T5862DRZ
tomo	47.7	20.3	rman	eman	-75.80	-114.66	doi:10.7283/T5BZ64B0
trve	2.5	5.6	rman	eman	-69.99	-67.55	doi:10.7283/T5NS0RZ9
ver1	0.3	100.0	prop	eman	-65.25	-64.26	SCAR
ver3	-6.2	100.0	prop	eman	-65.25	-64.26	SCAR
vnad	4.4	1.1	prop	prop	-65.25	-64.25	doi:10.7283/T52F7KQ1
w01b	1.4	10.0	prop	eman	-87.42	-149.44	
w02b	2.3	10.0	prop	eman	-85.61	-68.56	doi:10.7283/T5445JTQ
w03a	-1.4	10.0	prop	eman	-81.58	-28.40	doi:10.7283/T50C4T3D
w03b	1.7	10.0	prop	eman	-81.58	-28.40	
w05a	2.3	10.0	prop	eman	-80.04	-80.56	doi:10.7283/T57W69HP
w05b	7.4	10.0	prop	eman	-80.04	-80.56	doi:10.7283/T50C4T3D



w06a	-2.2	100.0	prop	eman	-79.63	-91.28	
w07a	3.3	100.0	prop	eman	-80.32	-81.43	
w08a	-1.5	100.0	prop	eman	-75.28	-72.18	
w09a	2.2	100.0	prop	eman	-82.68	-104.40	
wasa	0.6	3.2	prop	eman	-73.04	-13.41	Sweden
whn0	2.2	0.9	prop	prop	-79.85	154.22	doi:10.7283/T5R49P2M
whtm	7.7	0.8	prop	prop	-82.68	-104.39	doi:10.7283/T5ZP44DZ
wiln	4.9	0.9	prop	prop	-80.04	-80.56	doi:10.7283/T53F4MX9
* https://www.unavco.org/projects/project-support/polar/geodetic/benchmarks/sites/crar.html (accessed 1 June 2017)							
**Geoscience Australia GNSS archive at ftp://ftp.ga.gov.au/geodesy-outgoing/gnss/ as of 1 June 2017. See also Brown, N. and Woods, A., 2008. Antarctic Geodesy 2006 – 2007 Field Report. Geoscience Australia, Record 2009/32. 77pp.							
*** SCARP Campaign datasets, doi:10.7283/T5T151QB , doi:10.7283/T59P2ZZD , doi:10.7283/T5K35RZP . Also see https://gcmd.nasa.gov/records/GCMD_JCADM_USA_SCARP.html							



Table A.3. Comparison of ‘prop,eman’ GPS uplift rates for this study with rates from other studies.

	REGINA		Thomas et al. 2011		Argus et al. (2014)		Wolstencroft et al. (2015)	
	y^u	σ^u	y^u	σ^u	y^u	σ^u	y^u	σ^u
a351	-0.9	1.8	0.8	1.3	1.1	3.5		
a368	-0.2	1.2	0.4	1.0				
for1	-0.2	2.9	-1.4	0.8				
for2	-0.3	2.7	2.1	0.9				
fos1	3.1	1.3	2.1	0.4	2.9	1.2	3.9	1.1
ftp1	-2.2	3.4	2.1	2.8				
hton	4.8	3.7						
mbl1	2.5	3.0	0.6	1.5				
mbl2	2.3	10	0.2	4.1			6.4	0.9
rob1	5.4	5.1	7.5	2.6				
w01a(-howe)	-0.3	10	-2.5	1.7	0.9	1.2		
w01b	1.4	10	-3.1	1.7				
w02a(-pece)	0.3	10	2.8	1.2	-1.2	1.9		
w02b	2.3	10	0.5	1.9				
w03a	-1.4	10	-3.2	1.8	-1.1	2.4		
w03b	1.7	10	-1.7	1.8				
w04a	3.7	100	3.0	1.1				
w05a	2.3	10	3.5	2.0				
w05b	7.4	10	5.3	1.2				
w06a	-2.2	100	-2.2	2.4	-4.7	4.4		
w07a	3.3	100	3.3	2.1	4.6	3.1		
w08a(b/sugg)	-1.5	100	1.3	1.3				
w09a	2.2	100	4.5	2.6				



909 *A.5 Choice of GRACE cut-off degree and biasing*

In this study, we identify GRACE coefficients of CSR RL05 up to-degree and order 50 appropriate to yield the most robust gravity field rates over Antarctica. Figure A.3 provides another indication based on the degree-power spectrum of the geoid rates. It is visible that GFZ RL05 and CSR RL05 are very similar up to degree and order 50, where the power spectra show minima. For higher degrees, however, the power of the gravity field recovered with GRACE

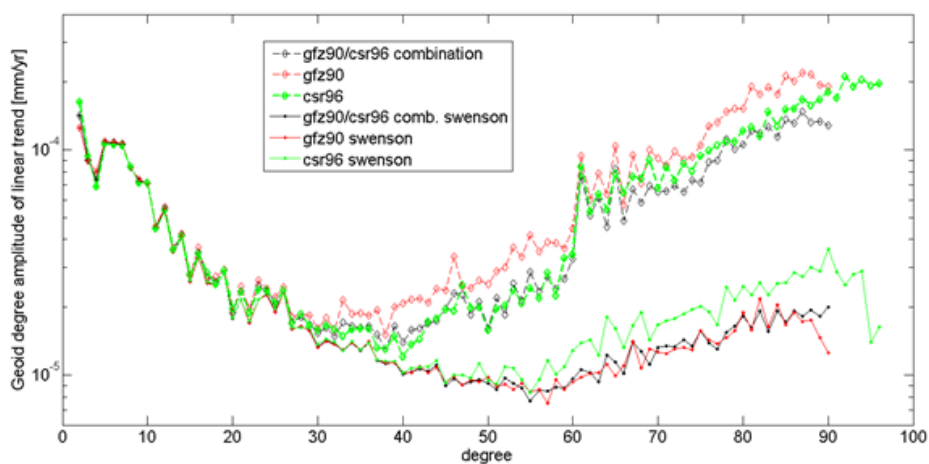


Figure A.3: Degree-amplitude spectrum of the rate of geoid-height change (mm/yr) for unfiltered (diamond-dashed lines) and for Swenson-filtered (solid lines) solutions. Red: GFZ; green: CSR; black combination of GFZ and CSR with equal weights.

915 increases due to increasing noise, for the unfiltered coefficients particularly faster for GFZ RL05 than for CSR RL05.

The filtering of the GRACE gravity fields was optimized for reducing noise over Antarctica. The effect on the RMS uncertainties is shown in Fig. 3. Additionally, Fig. A.4



presents the difference of between the GRACE rates filtered only with a Gaussian smoothing
filter of 200 km, and additionally with the optimized Swenson filter. It is visible that the
921 differences in the rate of geoid-height change and the associated rate of equivalent water-height
change, respectively, show a stripe-like noise pattern. This suggests that the de-stripping is
superior over conventional Gaussian smoothing, even at high latitudes, where GRACE ground-
924 track spacing is very dense. It is also important to note that the filter does not introduce any
magnitude bias, or changes the spectral content of the gravity field rates, which is important
when applying only Gaussian smoothing of 200 km (without Swenson filtering) to the altimetry
927 data set and response kernels.

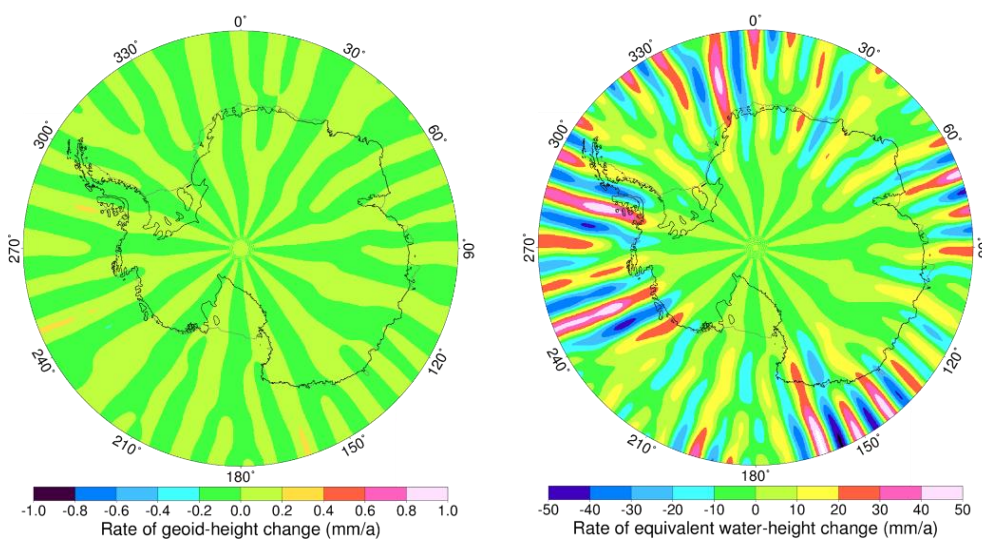


Figure A.4: Spatial rate of geoid-height change (left) and rate of equivalent water-height change (right) (mm/yr) for the difference between the GRACE trends processed by Gaussian smoothing of 200 km and the optimal Swenson filter & Gaussian smoothing. The solutions are CSR RL05, the spherical-harmonic cut-off degree is 50.



A.6 Evaluation of assumption of viscoelastic equilibrium state

930 The viscoelastic response kernels employed (Section 5) describe the viscoelastic
 equilibrium state for the forcing with a disc load of constant radius and constant rate of mass
 increase (likewise mass loss). We neglect transitional changes of the solid Earth for load
 933 changes that have not reached the equilibrium state in terms of geoid-height change and surface
 displacement. Although, the deformation and gravity signature in equilibrium eventually only
 depends on the lithosphere thickness, the time to reach the equilibrium is controlled by the
 936 viscosity parameters chosen. Fig. A.5 shows the evolution of the standardized ratio of the geoid-

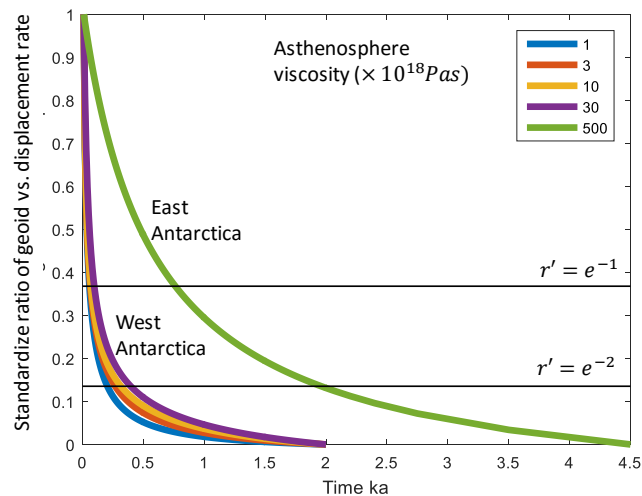


Figure A.5: Standardized ratio of the rate of geoid-height change versus the rate of radial displacement for different values of the asthenosphere viscosity. Note that the ratio is calculated at the load center.

height change vs. surface displacement over time, calculated as
 $r' = [r(t) - r(t = t_{max})] / \max[r(t) - r(t = t_{max})]$, where $r = y^g(t) / y^u(t)$ is



939 evaluated at the load centre. It is visible that for the weaker West Antarctic rheology
940 (asthenosphere viscosity between 1×10^{18} Pa s and 3×10^{19} Pa s) r' falls to $1/e^2$ within the
941 500 yr. For East Antarctica (1×10^{20} Pa s), $r' = e^{-2}$ is reached within 2 kyrs. With this quasi-
942 stationary solution approach, the inference on the timing of the past ice mass change is limited
943 to an upper limit in terms of magnitude, and a lower limit in terms of load duration; a similar
944 ratio is achieved by a thinner lithosphere thickness, which has not reached viscoelastic
945 equilibrium state, and earlier load changes are fully relaxed, respectively.

REFERENCES

948

- An, M., Wiens, D. A., Zhao, Y., Feng, M., Nyblade, A. A., Kanao, M., Li, Y., Maggi, A. &
Lévêque, J. J. (2015). S-velocity model and inferred Moho topography beneath the
951 Antarctic Plate from Rayleigh waves. *J. Geophys. Res.: Solid Earth*, 120(1), 359-383.
- Argus, D. F., Peltier, W. R., Drummond, R., & Moore, A. W. (2014). The Antarctica
component of postglacial rebound model ICE-6G_C (VM5a) based on GPS positioning,
954 exposure age dating of ice thicknesses, and relative sea level histories. *Geophys. J. Int.*,
198(1), 537-563.
- Bentley, M. J., Cofaigh, C. Ó., Anderson, J. B., Conway, H., Davies, B., Graham, A. G., &
957 others (2014). A community-based geological reconstruction of Antarctic Ice Sheet
deglaciation since the Last Glacial Maximum. *Quat. Sci. Rev.*, 100, 1-9.
- Bettadpur, S. (2012). Gravity Recovery and Climate Experiment UTCSR level-2 processing
960 standards document. University of Texas at Austin, *GRACE Doc*, 327742, 16.
- Bevis, M., Kendrick, E., Smalley, R., Dalziel, I., Caccamise, D., Sasgen, I., Helsen, M.,
Taylor, F. W., Zhou, H., Brown, A., Raleigh, D., Willis, M., Wilson, T. & Konfal, S.
963 (2009). Geodetic measurements of vertical crustal velocity in West Antarctica and the
implications for ice mass balance. *Geochemistry, Geophysics, Geosystems*, 10(10). doi:
10.1029/2009GC002642
- Borsa, A. A., Moholdt, G., Fricker, H. A., & Brunt, K. M. (2013). A range correction for
966 ICESat and its potential impact on ice sheet mass balance studies. *The Cryosphere
Discuss.*, 7, 4287-4319.
- Brenner, A. C., DiMarzio, J. P., & Zwally, H. J. (2007). Precision and accuracy of satellite
969 radar and laser altimeter data over the continental ice sheets. *IEEE Trans. Geosci.
Remote Sens.*, 45(2), 321-331.



- 972 Chambers, D. P., Bonin, J. A. (2012). Evaluation of Release-05 GRACE time-variable gravity
coefficients over the ocean. *Ocean Sci.*, 8, 859-868, 2012
- 975 Cheng, M., Tapley, B. D., & Ries, J. C. (2013). Deceleration in the Earth's oblateness. *J.
Geophys. Res.: Solid Earth*, 118(2), 740-747.
- Dahle, C. (2013). GFZ GRACE level-2 processing standards document for level-2 product
release 0005. *Deutsches GeoForschungsZentrum GFZ*,
978 <http://dx.doi.org/10.2312/GFZ.b103-1202-25>.
- Dobslaw, H.; Flechtner, F.; Bergmann-Wolf, I.; Dahle, Ch.; Dill, R.; Esselborn, S.; Sasgen, I.;
Thomas, M. (2013): Simulating high-frequency atmosphere-ocean mass variability for
981 de-aliasing of satellite gravity observations: AOD1B RL05. *J. Geophys. Res.*, doi:
10.1002/jgrc.20271.
- Dow, J.; Neilan, R; & Rizos C. (2009). The International GNSS Service in a changing
984 landscape of Global Navigation Satellite Systems. *Journal of Geodesy*, 83(3), 191-198.
- Duan, X. J., Guo, J. Y., Shum, C. K., & Van Der Wal, W. (2009). On the postprocessing
removal of correlated errors in GRACE temporal gravity field solutions. *Journal of*
987 *Geodesy*, 83(11), 1095-1106.
- Dubbini, M., Cianfarra, P., Casula, G., Capra, A. & Salvini, F. (2010). Active tectonics in
northern Victoria Land (Antarctica) inferred from the integration of GPS data and
990 geologic setting. *J. Geophys. Res.: Solid Earth*, 115.
- Dziewonski, A. M., & Anderson, D. L. (1981). Preliminary reference Earth model. *Phys. Earth
Planet. Inter.*, 25(4), 297-356.
- 993 Flament, T., & Rémy, F. (2012). Dynamic thinning of Antarctic glaciers from along-track
repeat radar altimetry. *J. Glaciol.*, 58(211), 830-840.
- 996 Gunter, B. C., Didova, O., Riva, R. E. M., Ligtenberg, S. R. M., Lenaerts, J. T. M., King, M.
A., van den Broeke, M. & Urban, T. (2014). Empirical estimation of present-day
Antarctic glacial isostatic adjustment and ice mass change. *The Cryosphere*, 8(2), 743-
760
- 999 Heeszel, D. S., Wiens, D. A., Anandakrishnan, S., Aster, R. C., Dalziel, I. W., Huerta, A. D.,
Nyblase, A. A., Wilson, T. J. & Winberry, P. (2016). Upper mantle structure of central and
West Antarctica from array analysis of Rayleigh wave phase velocities. *J. Geophys. Res.:
1002 Solid Earth*, doi: 10.1002/2015JB012616.
- Heiskanen, W. A., & Moritz, H. (1967). Physical geodesy. *Bulletin Géodésique (1946-1975)*,
86(1), 491-492.
- 1005 Hofton, M. A., Luthcke, S. B., & Blair, J. B. (2013). Estimation of ICESat intercampaign
elevation biases from comparison of lidar data in East Antarctica. *Geophys. Res. Lett.*,
40(21), 5698-5703.
- 1008 Horwath, M., Legrésy, B., Rémy, F., Blarel, F., & Lemoine, J. M. (2012). Consistent patterns
of Antarctic ice sheet interannual variations from ENVISAT radar altimetry and GRACE
satellite gravimetry. *Geophys. J. Int.*, 189(2), 863-876.



- 1011 Howat, I. M., Smith, B. E., Joughin, I., & Scambos, T. A. (2008). Rates of southeast Greenland ice volume loss from combined ICESat and ASTER observations. *Geophys. Res. Lett.*, 35(17), L17505.
- 1014 Hurkmans, R. T. W. L., Bamber, J. L., Sørensen, L. S., Joughin, I. R., Davis, C. H., & Krabill, W. B. (2012). Spatiotemporal interpolation of elevation changes derived from satellite altimetry for Jakobshavn Isbræ, Greenland. *J. Geophys. Res.: Earth Surface*, 117(F3).
- 1017 Ivins, E. R., & James, T. S. (2005). Antarctic glacial isostatic adjustment: a new assessment. *Antarct. Sci.*, 17(04), 541-553.
- 1020 Konrad, H., Sasgen, I., Pollard, D., & Klemann, V. (2015). Potential of the Solid-Earth response for limiting long-term West Antarctic Ice Sheet retreat in a warming climate. *Earth Planet. Sci. Lett.*, 432, 254-264.
- 1023 Lenaerts, J. T. M., den Broeke, M. R., Berg, W. J., Meijgaard, E., & Kuipers Munneke, P. (2012). A new, high-resolution surface mass balance map of Antarctica (1979–2010) based on regional atmospheric climate modeling. *Geophys. Res. Lett.*, 39(4).
- 1026 Ligtenberg, S. R. M., Heisen, M. M., & van de Broeke, M. R. (2011). An improved semi-empirical model for the densification of Antarctic firn. *The Cryosphere*, 5(4), 809-819.
- Martinec, Z. (2000). Spectral–finite element approach to three-dimensional viscoelastic relaxation in a spherical earth. *Geophys. J. Int.*, 142(1), 117-141.
- 1029 Martín-Español, A., Zammit-Mangion, A., Clarke, P. J., Flament, T., Helm, V., King, M. A., Luthcke, S. B., Petrie, E., Rémy, F., Schön, N. et al. (2016a), Spatial and temporal Antarctic Ice Sheet mass trends, glacio-isostatic adjustment, and surface processes from a joint inversion of satellite altimeter, gravity, and GPS data, *J. Geophys. Res. Earth Surf.*, 121, 182–200, doi:10.1002/2015JF003550.
- 1032
- 1035 Martín-Español, A., King, M. A., Zammit-Mangion, A., Andrews, S. B., Moore, P. & Bamber J. L. (2016b), An assessment of forward and inverse GIA solutions for Antarctica, *J. Geophys. Res. Solid Earth*, 121, 6947–6965, doi:10.1002/2016JB01315.
- 1038 Moholdt, G., Nuth, C., Hagen, J. O., & Kohler, J. (2010). Recent elevation changes of Svalbard glaciers derived from ICESat laser altimetry. *Remote Sens. Environ.*, 114(11), 2756-2767.
- 1041 Morelli, A., & Danesi, S. (2004). Seismological imaging of the Antarctic continental lithosphere: a review. *Global Planet. Change*, 42(1), 155-165.
- 1044 Mouginit, J., Rignot, E., & Scheuchl, B. (2014). Sustained increase in ice discharge from the Amundsen Sea Embayment, West Antarctica, from 1973 to 2013. *Geophys. Res. Lett.*, 41(5), 1576-1584.
- 1047 Nield, G. A., Whitehouse, P. L., King, M. A., Clarke, P. J., & Bentley, M. J. (2012). Increased ice loading in the Antarctic Peninsula since the 1850s and its effect on glacial isostatic adjustment. *Geophys. Res. Lett.*, 39(17).
- 1050 Nield, G. A., Barletta, V. R., Bordoni, A., King, M. A., Whitehouse, P. L., Clarke, P. J., Domack, E., Scambos, T. A., Berthier, E. (2014). Rapid bedrock uplift in the Antarctic Peninsula explained by viscoelastic response to recent ice unloading. *Earth Planet. Sci. Lett.*, 397, 32-41.



- 1053 Peltier, W. R., & Andrews, J. T. (1976). Glacial-isostatic adjustment—I. The forward problem. *Geophysical Journal International*, 46(3), 605-646.
- Peltier, W. R. (2004). Global glacial isostasy and the surface of the ice-age Earth: The ICE-5G (VM2) model and GRACE. *Annu. Rev. Earth Planet. Sci.*, 32, 111-149.
- 1056 Priestley, K., & McKenzie, D. (2013). The relationship between shear wave velocity, temperature, attenuation and viscosity in the shallow part of the mantle. *Earth Planet. Sci. Lett.*, 381, 78-91.
- 1059 Ranalli, G., & Murphy, D. C. (1987). Rheological stratification of the lithosphere. *Tectonophysics*, 132(4), 281-295.
- 1062 Raymond, C. A., E. R. Ivins, M. B. Heflin and T. S. James, (2004). Quasi-continuous global positioning system measurements of glacial isostatic deformation in the northern Transantarctic Mountains. *Glob. Plant. Change*, 42, 295-303.
- 1065 Retzlaff, R., and C. Bentley (1993), Timing of stagnation of Ice Stream C, West Antarctica, from short-pulse radar studies of buried surface crevasses, *J. Glaciol.*, 39(133), 533–561.
- 1068 Rignot, E., Mouginot, J., Morlighem, M., Seroussi, H., & Scheuchl, B. (2014). Widespread, rapid grounding line retreat of Pine Island, Thwaites, Smith, and Kohler glaciers, West Antarctica, from 1992 to 2011. *Geophys. Res. Lett.*, 41(10), 3502-3509.
- 1071 Riva, R. E., Gunter, B. C., Urban, T. J., Vermeersen, B. L., Lindenbergh, R. C., Helsen, M. M., Bamber, J. L., van de Wal, R., van den Broeke, M. R. & Schutz, B. E. (2009). Glacial isostatic adjustment over Antarctica from combined ICESat and GRACE satellite data. *Earth Planet. Sci. Lett.*, 288(3), 516-523.
- 1074 Sasgen, I., Martinec, Z., & Fleming, K. (2006). Wiener optimal filtering of GRACE data. *Stud Geophys Geod.*, 50(4), 499-508.
- 1077 Sasgen, I., Dobsław, H., Martinec, Z., & Thomas, M. (2010). Satellite gravimetry observation of Antarctic snow accumulation related to ENSO. *Earth Planet. Sci. Lett.*, 299(3), 352-358.
- 1080 Sasgen, I., Konrad, H., Ivins, E. R., Van den Broeke, M. R., Bamber, J. L., Martinec, Z., & Klemann, V. (2013): Antarctic ice-mass balance 2003 to 2012: regional reanalysis of GRACE satellite gravimetry measurements with improved estimate of glacial-isostatic adjustment based on GPS uplift rates, *The Cryosphere*, 7, 1499-1512, doi:10.5194/tc-7-1499-2013.
- 1083 Sasgen, I., Martín-Español, A., Horvath, A., Klemann, V., Petrie, E.J., Wouters, B., Horvath, M., Pail, R., Bamber, J.L., Clarke, P.J., Konrad, H. & Drinkwater, M. R., Estimate of regional glacial isostatic adjustment in Antarctica considering a lateral varying Earth structure – Part II: data combination and impact analysis (ESA STSE Project REGINA), *Geophys. J. Int.*, submitted.
- 1086
- 1089 Scambos, T., and C. Schuman (2016), Comment on 'Mass gains of the Antarctic ice sheet exceed losses' by H. J. Zwally and others, *J. Glaciol.*, 62, 599–603, doi:10.1017/jog.2016.59.



- 1092 Schotman, H. H. A., Wu, P., & Vermeersen, L. L. A. (2008). Regional perturbations in a
global background model of glacial isostasy. *Physics of the Earth and Planetary Interiors*,
171(1), 323-335.
- 1095 Schroeder, D. M., Blankenship, D. D., Young, D. A., & Quartini, E. (2014). Evidence for
elevated and spatially variable geothermal flux beneath the West Antarctic Ice Sheet.
Proceedings of the National Academy of Sciences, 111(25), 9070-9072.
- 1098 Shapiro, N. M., & Ritzwoller, M. H. (2004). Inferring surface heat flux distributions guided
by a global seismic model: particular application to Antarctica. *Earth Planet. Sci. Lett.*,
223(1), 213-224.
- 1101 Shepherd, A. (2012). A reconciled estimate of ice-sheet mass balance, *Science*, 338(6114),
1539-1539.
- 1104 Sjöberg, L., Walyeldeen, H. & Horemuz, M. (2011). Estimation of Crustal Motions at the
Permanent GPS Station SVEA, Antarctica from 2005 to 2009. *J. Geod. Sci.* 1(3): 215-
220, doi:10.2478/v10156-010-0024-1.
- Swenson, S., & Wahr, J. (2006). Post-processing removal of correlated errors in GRACE data.
Geophys. Res. Lett., 33(8), L08402.
- 1107 Thomas, I. D., King, M. A., Bentley, M. J., Whitehouse, P. L., Penna, N. T., Williams, S. D. P.,
Riva, R. E. M., Lavalée, D. A., Clarke, P. J., King, E. C. & others (2011). Widespread
low rates of Antarctic glacial isostatic adjustment revealed by GPS observations.
1110 *Geophys. Res. Lett.*, 38(22), L22302. doi: 10.1029/2011gl049277
- van der Wal, W., Whitehouse, P. L., & Schrama, E. J. (2015). Effect of GIA models with 3D
composite mantle viscosity on GRACE mass balance estimates for Antarctica. *Earth*
1113 *Planet. Sci. Lett.*, 414, 134-143.
- van Ommen, T. D., Morgan, V., & Curran, M. A. (2004). Deglacial and holocene changes in
accumulation at Law Dome, East Antarctica. *Annals of Glaciology*, 39(1), 359-365.
- 1116 Wahr, J., Wingham, D., & Bentley, C. (2000). A method of combining ICESat and GRACE
satellite data to constrain Antarctic mass balance. *J. Geophys. Res.: Solid Earth*, 105(B7),
16279-16294.
- 1119 Wan, H., Giorgetta, M. A., Zängl, G., Restelli, M., Majewski, D., Bonaventura, L., Fröhlich,
K., Reinert, D., Rípodas, P., Kornbluh, L., and Förstner, J. (2013), The ICON-1.2
hydrostatic atmospheric dynamical core on triangular grids – Part 1: Formulation and
1122 performance of the baseline version, *Geosci. Model Dev.*, 6, 735-763, doi:10.5194/gmd-
6-735-2013, 2013.
- 1125 Wessel, P., Smith, W. H. F., Scharroo, R., Luis, J. F. and Wobbe, F. Generic Mapping Tools:
Improved version released, *EOS Trans. AGU*, 94, 409-410, 2013.
- Williams, S. (2008). CATS: GPS coordinate time series analysis software. *GPS Solutions*
12(2): 147-153.
- 1128 Whitehouse, P. L., Bentley, M. J., Milne, G. A., King, M. A., and Thomas, I. D. (2012): A new
glacial isostatic adjustment model for Antarctica: calibrated and tested using observations
of relative sea-level change and present-day uplift rates, *Geophys. J. Int.*, 190, 1464–
1131 1482, doi:10.1111/j.1365-246X.2012.05557.x.



- 1134 Wolstencroft, M., King, M. A., Whitehouse, P. L., Bentley, M. J., Nield, G. A., King, E. C.,
McMillan, M., Shepherd, A., Barletta, V., Bordon, A. & others (2015). Uplift rates from
a new high-density GPS network in Palmer Land indicate significant late Holocene ice
loss in the southwestern Weddell Sea. *Geophys. J. Int.*, 203(1), 737-754.
- 1137 Wouters, B., Bonin, J. A., Chambers, D. P., Riva, R. E. M., Sasgen, I., & Wahr, J. (2014).
GRACE, time-varying gravity, Earth system dynamics and climate change. *Rep. Prog.
Phys.*, 77(11), 116801.
- 1140 Wu, X., Heflin, M. B., Schotman, H., Vermeersen, B. L., Dong, D., Gross, R. S., Ivins, E. R.,
Moore, A. W. & Owen, S. E. (2010). Simultaneous estimation of global present-day water
transport and glacial isostatic adjustment. *Nat. Geosci.*, 3(9), 642-646.